Spin polarization and superconductivity in Andreev point contacts

van Tilborg, J.

Award date:
2001

Eindhoven University of Technology
Department of Applied Physics
Group Physics of Nanostructures

Spin Polarization and Superconductivity in Andreev Point Contacts

J. van Tilborg

June, 2001

Report of a graduation project.
Supervisors: Ir. C.H. Kant, Dr. O. Kurnosikov and Dr. Ir. H.J.M. Swagten.
Professor: Prof. Dr. Ir. W.J.M. de Jonge.

Abstract

In order to study spin polarization via the phenomenon of Andreev Reflection at a normal-metal/superconductor (N/S) interface, current-voltage measurements have been performed on ballistic N/S point contacts. A piezo system realizes the contact formation by approaching a superconducting tip onto a sample. This report focuses only on those results that resemble the modified Blonder-Tinkham-Klapwijk model, valid for ballistic contacts. By fitting the measurements with this model, one can extract the superconducting bandgap Δ, the parameter Z which incorporates interfacial scattering, and the degree of spin polarization P.

Measurements on Co/Nb and Co/Pb contacts yield $P \simeq 45\%$ (as observed by other groups) for contacts with low Z. However, the measured P decreases for contacts with higher Z, which can be attributed to enhanced spin-flip scattering in this regime.

Furthermore, a measurement series on a single Co/Nb contact shows an exponential decay in the bandgap as a function of contact resistance. This effect is confirmed by an intuitive model, based on the idea that the superconducting Cooper pairs are confined by tip geometry with a sharpness on the scale of the coherence length.

Measurements on Au/Pb show that the current through the contact is able to generate fields larger than this critical value. The observations are consistent with the model proposed by Westbrook and Javan, allowing to obtain an estimate for H_c, which is about 30 times smaller than the bulk value.

Contents

1 General introduction

1.1 Magnetic nanostructures

The main subject discussed in this report is part of a large and growing field of research, namely the physics of magnetic nanostructures. Over the past two decades new developments in deposition technology made this field of research attractive for further investigation [Strij99].

The giant and tunneling magnetoresistance effect

Two major breakthroughs in the field were the discovery in 1988 of the giant magnetoresistance (GMR) effect and the first demonstration in 1995 of the tunneling magnetoresistance (TMR) effect. The basics of the GMR effect [Bai88] are shown in Figure 1. A current, consisting of spin-up and spin-down electrons, enters a system of two magnetic layers separated by a non-magnetic layer. The relative orientation of the electron's spin with respect to the magnetization plays a crucial role in determining the resistance of the structure. If this spin/magnetization orientation is parallel, few scattering events will occur, resulting in a low resistance. A high resistance is the result of an anti-parallel spin/magnetization orientation, since at this orientation many scattering events occur.

A second crucial part for existence of the GMR effect is the orientation of the magnetizations of the two magnetic layers. If the directions of magnetization are anti-parallel, the total resistance will end up higher than in the parallel case. This can been seen if one calculates the equivalent resistance for the two schemes in Figure 1. For the equivalent resistance in the parallel magnetization scheme, one can deduce $R_P = (2R_{small}R_{large})/(R_{small} + R_{large})$. In the anti-parallel case, this corresponds to $R_{AP} = (R_{small} + R_{large})/2$. Simple calculations can prove that $R_{AP} \geq R_P$ (one channel is shorted in the parallel case). The existence of this resistance difference is referred to as the GMR effect, and the convention for its magnitude reads $GMR(\%) = (R_{AP} - R_P)/(R_P) \cdot 100$.

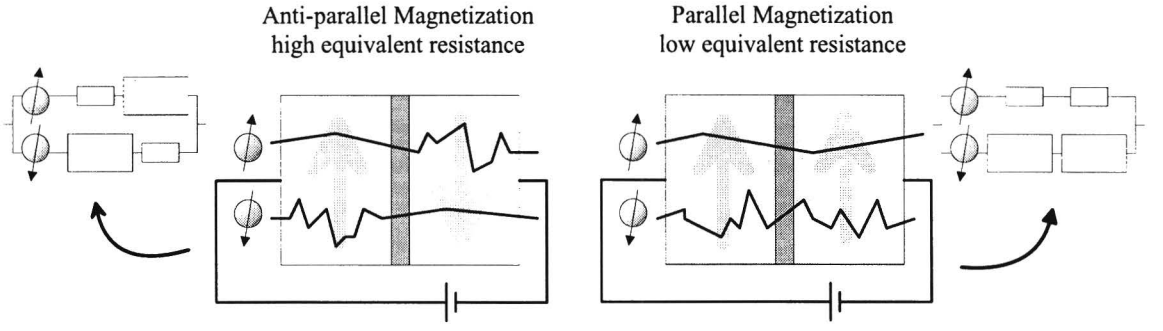

Figure 1: Illustration of spin-dependent scattering and its consequence (GMR effect). Spin-up and spin-down electrons traverse two magnetic materials separated by a non-magnetic layer. The amount of collisions determines the magnitude of the resistance in the two resistance schemes (the magnitude is represented by size).

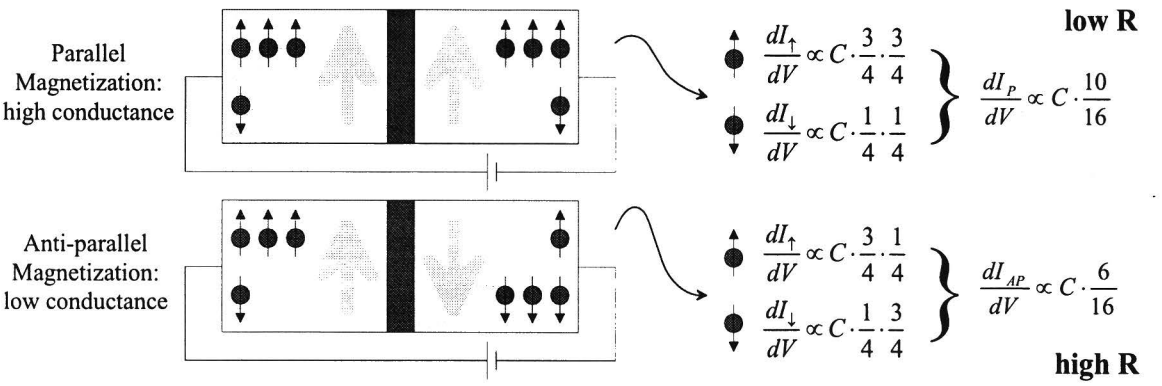

Figure 2: Illustration of the origin of the TMR effect. Two magnetic materials (the distribution of majority and minority spins is 75%-25%) are separated by an insulator. A parallel orientation of the two magnetizations results in a higher conductance than an anti-parallel orientation.

The demonstration of the TMR effect [Moo95] shows two magnetic materials, separated by an insulating layer (Figure 2). As is valid for all magnetic materials, the electrons that contribute to the current are not equally distributed over the two spin orientations (the number of spin-up electrons $N_\uparrow$ is not equal to the number of spin-down electrons $N_\downarrow$). In the example of Figure 2, the spin orientation parallel to the magnetic field has a majority population of 75%.

In spite of the existence of an insulating barrier in the system in Figure 2, a current can flow due to electron tunneling. Following the simplified approach by Julliere [Jul75], the chance that an electron with spin σ can tunnel through the barrier is referred to as the tunneling probability T_σ and is given by $T_\sigma \sim N_\sigma^{Left} \cdot N_\sigma^{Right}$. Therefore, the conductance contribution $G_\sigma = \frac{dI_\sigma}{dV}$ of a certain spin orientation reads $G_\sigma \sim G_\sigma^{left} \cdot G_\sigma^{right}$. Calculating the total conductance $G = G_\uparrow + G_\downarrow$, one will find a higher value in the parallel orientation of the two magnetic layers than in the anti-parallel orientation. Therefore, the resistance R_P in the parallel orientation is lower than the resistance R_{AP} in the anti-parallel orientation. This difference is referred to as the TMR effect and a magnitude for the effect is given by $TMR(\%) = \frac{R_{AP}-R_P}{R_P} \cdot 100$.

Application of the effects

The ability to externally switch the orientation of the two magnetic layers (in both the GMR and TMR effect), is crucial for various attractive industrial applications [Pri95]. The switching simply alters the resistance of the structure. Roughly spoken, one can use the dependency of the resistance to the relative magnetic orientation as an effect to read or write bits (a high or low resistance can symbolize a 0 or 1).

GMR structures are used in the newest generation of hard-disk read heads, and the TMR structures are currently being developed for the non-volatile storage of information in a so-called magnetic RAM. The term 'non-volatile' indicates the conservation of infor-

mation, even if no power is supplied to the system.

1.2 Spin Polarization

Spin polarization in the GMR and TMR effect

The previous section introduced two interesting effects, both concerning electron movement in magnetic structures. The physics behind the effects is far more complex, and for a great deal not understood yet. One subject that is of importance is the so-called spin polarization of the magnetic materials. A material is spin polarized if the number of spin-up electrons $N_\uparrow$ that contribute to the current is not equal to the number of contributing spin-down electrons $N_\downarrow$. As will be discussed in the next paragraph, only electrons with energy equal to the Fermi energy E_F contribute to the current. A frequently used formula for the magnitude of spin polarization (or the degree of spin polarization) P_N is given by

$$P_N = \frac{N_\uparrow(E_F) - N_\downarrow(E_F)}{N_\uparrow(E_F) + N_\downarrow(E_F)}. \tag{1}$$

All known magnetic materials have a degree of spin polarization $P_N \neq 0$. An upper-bound for $|P_N|$ is realized in a magnetic material in which all electrons have the same spin orientation, and is given by $|P_N| = 1$.

Spin polarization at the Fermi level

One might wonder why the electrons with Fermi energy play the crucial part in the definition for P_N, and not electrons with lower (other) energies. The following approach gives insight to the answer. Electrons in a metal are distributed over all energies E according to the Fermi-Dirac distribution $f(E)$, plotted in Figure 3. The interval over which the function $f(E)$ drops from 1 to 0 zero is characterized by a width kT, with k=86 μeV/K and T the temperature. The transport of the electrons through the material (i.e. the current) is dependent on (a) the energy of the electron, (b) the chance $f(E)$ this energy state is occupied and (c) the chance 1-$f(E)$ a similar state is empty. The previous results in the equation: $I(E) \sim f(E) \cdot [1 - f(E)]$.

The function $f(E) \cdot [1 - f(E)]$ is plotted in Figure 3 (T=293 K and E_F=5 eV). The curve shows that only electrons with energy $|E - E_F| < kT$ contribute to the current. Since even at room temperature $kT/E_F \ll 1$, one can replace the condition $|E - E_F| < kT$ by $E \simeq E_F$. Therefore the degree of spin polarization (DSP) at this energy level is of key importance.

Direct methods for probing the spin polarization

Application of spin polarized materials automatically leads to the need of being able to directly measure its magnitude. In this respect, techniques relying on magnetic switching (as discussed previous) are examples of indirect probing methods and do not satisfy this

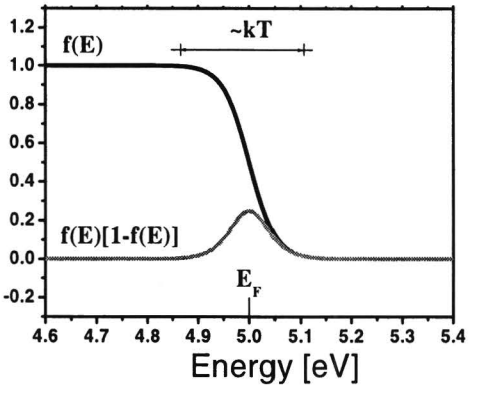

Figure 3: Construction of the function $f(E) \cdot [1 - f(E)]$ at room temperature, with $f(E)$ the Fermi-Dirac distribution. Even at room temperature ($kT \simeq 25$ meV), only electrons with energy approximately equal to the Fermi energy (typical $E_F \approx 5$ eV) contribute to the current.

need. Furthermore, these techniques involve two magnetic materials with all additional problems associated (physics not well understood).

For the direct measurement of the spin polarization, three methods are used, namely Spin-polarized Tunneling, Andreev Reflection and Electron Photo-emission (Figure 4).

With the latter technique, electrons with energies within a tunable energy range are scattered out of the metal. A Mott detector (named after Sir N.F. Mott) counts the number of spin-up and spin-down electrons separately. A disadvantage of this technique is the poor (with respect to the two other techniques) energy resolution that is obtained. Furthermore, the setup for the Mott detector is large and complex.

The two other techniques are based on conductance measurements. In such experiments, the conductance dI/dV through a system is measured as a function of applied voltage V. Comparing the measured data with theory, one can extract the degree of spin polarization. Spin-polarized Tunneling requires a magnetic field of several Tesla, pumped liquid ^{3}He-temperature (typically 0.3 K) and 'high quality' tunnel junctions [Mes94]. The values for the field B and temperature T are the consequence of measuring the Zeeman

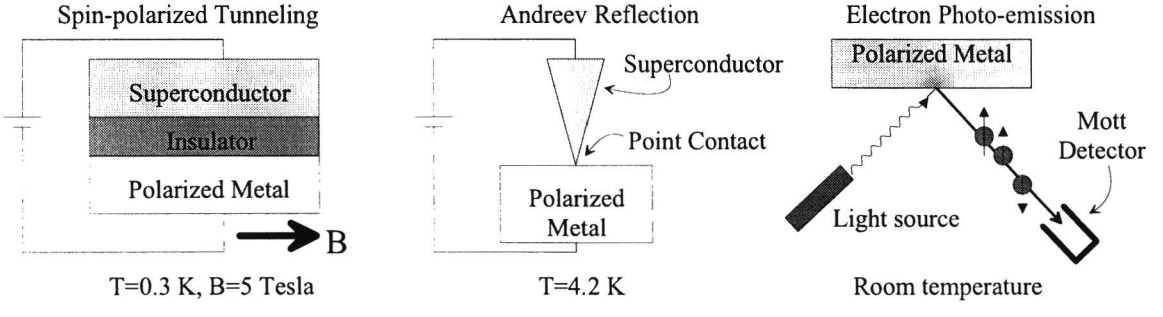

Figure 4: Three methods for probing spin polarization in a normal metal.

splitting μB, which is experimentally only possible if $\mu B \gg kT$ (μ=60 μeV/Tesla and k=86 μeV/Kelvin).

The contents of this report discusses Andreev Reflection. With this method one measures the conductance through a point contact between a superconducting metal and a normal metal. A point contact is defined as a contact with a small radius a compared to the electron's mean free path l ($a \ll l$). Determining the DSP from conductance curves requires $kT \ll \Delta$ (see Section 3.4), with Δ the superconducting bandgap, to be introduced in Section 2.3 (typically $\Delta \simeq 1$ meV). Liquid ^{4}He-temperatures (typically 1.2-4.2 K) satisfy this demand. A restriction to this technique is the fact that only the magnitude of the spin polarization can be determined and not its sign (one can not determine if the majority spin has orientation spin-down or spin-up).

1.3 Andreev Reflection

The idea of using Andreev Reflection [And64] for probing spin polarization was first proposed by de Jong and Beenakker [Jong95]. Andreev Reflection occurs at the boundary of a normal metal and a superconducting metal. The origin of the effect can be found in the fact that, in a simplified picture, electrons in a superconductor are obliged to form pairs, the so-called Cooper pairs. A Cooper pair consists of a spin-up and a spin-down electron, both with equal but opposite momenta. What happens to the electrons in a normal metal when they reach the boundary with a superconductor is shown in Figure 5. Coming from a nonpolarized normal metal ($N_\uparrow(E_F)$=$N_\downarrow(E_F)$), a spin-up electron can easily find a spin-down electron and form a Cooper pair in the superconductor. Consequently, a relatively high current can flow. The pair-forming process is called Andreev Reflection since the process of combining of the initial and second electron is equivalent to reflection

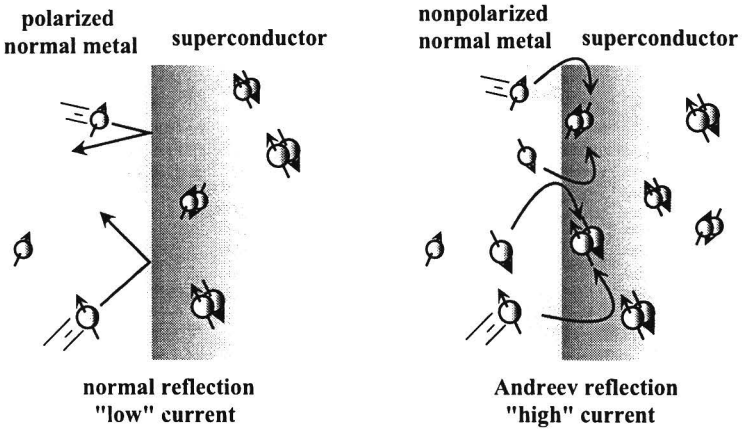

Figure 5: Electrons coming from a 100%-polarized normal metal (left) can not form Cooper pairs, which makes Andreev Reflection impossible to occur. At the interface between the superconductor and a nonpolarized normal metal (right), Andreev Reflection has its maximum chance of occurrence and the current flowing through this system will be relatively high.

of the initial electron as a hole. In a nonpolarized-N/S contact it has a maximum chance of occurrence. However, the spin-up electrons in a highly polarized normal metal have a hard time pairing with a spin-down electron for the simple reason that spin-down electrons hold the minority. In this case, Andreev Reflection has a small chance of occurrence and the electrons coming from the polarized normal metal are forced to reflect back. In other words: the magnitude for the current though a normal-metal/superconductor contact is determined by the DSP.

1.4 Author's contribution to previous work

All research described in the following chapters is part of a project initiated in August 1999. After defining the experimental goals, the first milestone was the realization of the experimental setup for measuring the conductance through point contacts at low temperatures (4.2 K). This phase, prior to the work that is described in this report, was finished by reaching a second highlight, namely preliminary measurements consistent with a theoretical model for normal-metal/superconductor nanocontacts. Superconducting properties, contact characteristics and the zero-polarization of Au could be determined by comparison with the theoretical model.

All work done in this first phase of the project is well described in [Kant00] and forms the base for the second phase described in this report. Over a period of time, several improvements to the setup have been made. One of them concerns the ability to reach temperatures of $\simeq 1.4$ K (in stead of 4.2 K). Operation at such a low temperature reduces vibrations, minimizes the effect of thermal smearing on measured conductance curves, and permits a wider range of applicable superconductors. Furthermore, several changes in the piezo system (the system responsible for contact formation) have improved the reliability considerably (the chance of malfunction has reduced to practically zero).

In the second phase, successful measurements of the spin polarization of Co have been performed. Furthermore, it has successfully been demonstrated that one can measure a series of conductance curves on a single stable contact, while changing the pressure of the tip on the sample.

1.5 Outline

The outline of this report is as follows. Chapter 2 will give an introduction to various characteristics of normal metals (and their magnetic properties), superconductors, and to the physics behind contacts in general. Two models for superconducting behaviour in N/S contacts are treated in more detail. The Blonder-Tinkham-Klapwijk model, which describes the electron transport through a ballistic nonpolarized-N/S contact, is treated in Chapter 3. The same chapter introduces a modification to the model, allowing the study of conductance through polarized-N/S contacts as well. An overview of the experimental setup is given in Chapter 4, in which the piezo system and the cooling procedure are described. In addition, attention is given to tip and sample preparation. The results are

discussed in Chapter 5, after which Chapter 6 presents the conclusions as well as suggestions for future research.

2 An introduction to normal metals, superconductors, and point contact properties

In the first section of this chapter, properties of electrons in metals are discussed. This will lead to a more formal introduction of spin polarization than the one given in Chapter 1. After this, insight in contact properties is given. Section 2.3 introduces the physics behind superconductivity. Since the destruction of superconductivity is observed in the experiments, attention to this subject is given in Section 2.4. The last section focuses on the decay of the superconducting bandgap if the contact is small compared to the superconducting coherence length.

2.1 Magnetic properties: magnetization and spin polarization

Electron distribution over energy

Various material properties depend on how the electrons are distributed over all allowed energies. Electrons prefer to fill up states with low energy but Pauli's exclusion principle prohibits the existence of two electrons in the same quantum state. The distribution of the number of electrons over the energy is governed by two factors: the number of available states at a certain energy(band) and the probability that these states will be occupied. The first factor is referred to as the density of states $N(E)$ and the second factor is given by the Fermi-Dirac distribution

$$f(E) = \frac{1}{\exp\left[(E - E_F)/(kT)\right] + 1}, \tag{2}$$

where E_F stands for the Fermi energy, T for the absolute temperature and k for Boltzman's constant (k=86 μeV/K). For $T = 0$ K, Equation 2 reduces to a step function, with $f(E) = 1$

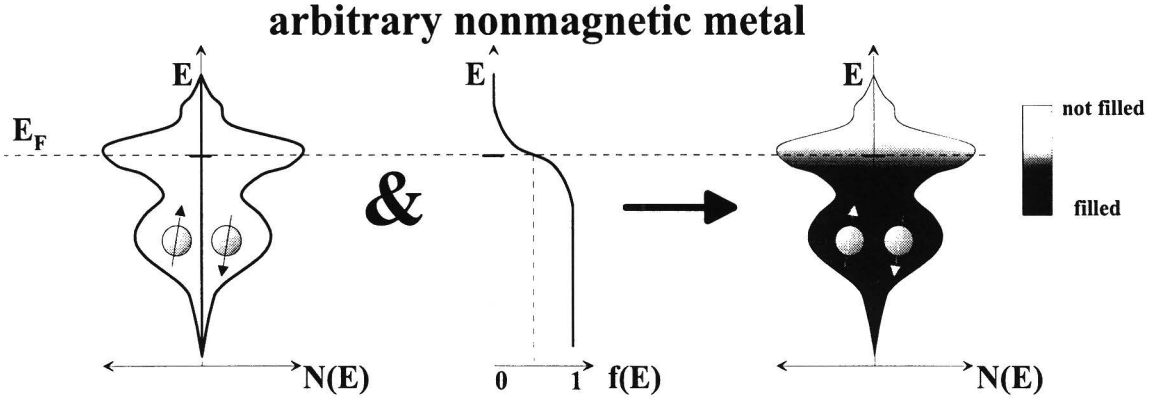

Figure 6: The left image shows an example of the density of states for a nonmagnetic normal metal. This plot can be combined with the Fermi-Dirac distribution $f(E)$ (middle image) to form the right image, predicting the number of electrons at a certain energy.

for $E \leq E_F$ and $f(E) = 0$ for $E > E_F$. For $T > 0$, states above E_F have a nonzero occupation probability.

In Figure 6, a fictitious DOS (density of states) is shown (left plot) for both spin-up and spin-down electrons. It is also shown how the DOS combined with the Fermi-Dirac distribution $f(E)$ (middle image) can predict the number of electrons at a certain energy (right plot).

Magnetization

In a metal, one can simply determine the net magnetization by summing up the magnetic moment of each individual electron. The total magnetic moment per unit volume is referred to as the magnetization of the material. One has to realize that the contribution of a spin-up electron will cancel out the contribution of a spin-down electron. The magnetization M can be calculated through

$$M \sim \left(\int^{E} f(E) N_{\uparrow}(E) dE - \int^{E} f(E) N_{\downarrow}(E) dE \right). \tag{3}$$

By interpreting Equation 3 it is obvious why a material like the one in Figure 6 has a zero magnetization: the DOS are equal for spin-up and spin-down electrons. In a magnetic metal however, the DOS for spin-up and spin-down electrons are shifted with respect of each other. For common magnetic metals, this shift amounts to h and $-h$ for each spin orientation, as indicated in Figure 7. For such a metal it is obvious that Equation 3 yields a nonzero magnetization.

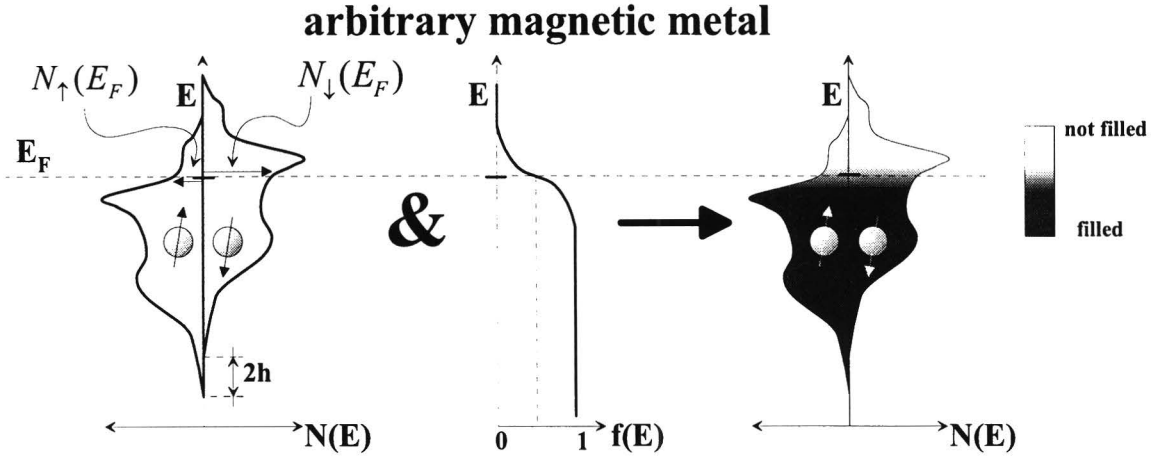

Figure 7: The left image shows an example of the density of states for a magnetic metal. The DOS for the two spin orientations are shifted with respect to each other, resulting in a netto magnetization.

Spin polarization

Another difference between the energy diagrams of Figures 6 and 7 is the density of states at the Fermi energy E_F. In Figure 6 one can see that $N_\uparrow(E_F) = N_\downarrow(E_F)$, while in Figure 7 $N_\uparrow(E_F) \neq N_\downarrow(E_F)$. A difference in the DOS for spin-up and spin-down electrons at this energy level is referred to as spin polarization. Section 1.2 discussed why this particular energy level E_F is of key importance (it was derived that only electrons with $E \simeq E_F$ contribute to the current). A common way to express the imbalance in the number of spin-up and spin-down electrons, is through the 'N-definition' DSP, given by

$$P_N = \frac{N_\uparrow(E_F) - N_\downarrow(E_F)}{N_\uparrow(E_F) + N_\downarrow(E_F)}. \tag{4}$$

Note that $|P| \leq 1$, with $P=0$ for nonpolarized materials and $|P|=1$ for fully polarized materials. All known magnetic metals are spin polarized at the Fermi level ($P_N \neq 0$).

Mazin [Maz99] shows that the spin-dependent signal in conductance measurements in the ballistic regime (the signal is the current) is not defined by the DOS alone, which makes the N-definition for the DSP useless. Since for a ballistic contact $I_{\uparrow(\downarrow)} \sim N_{F\uparrow(\downarrow)} v_{F\uparrow(\downarrow)}$ (DOS and velocity at Fermi level!), one can derive a second definition for DSP, namely P_{Nv}, which is given by

$$P_{Nv} = \frac{N_{F\uparrow} v_{F\uparrow} - N_{F\downarrow} v_{F\downarrow}}{N_{F\uparrow} v_{F\uparrow} + N_{F\downarrow} v_{F\downarrow}}. \tag{5}$$

To give some examples: bandgap calculations show P_N=0.36 for LSMO ($La_{0.7}Sr_{0.3}MnO_3$), while conductance measurements on point contacts yield $P_{Nv} = 0.8$ [Nad00]. Metals in which the current is (nearly) fully polarized ($P_{Nv} \simeq 1$) are referred to as transport half-metals. LSMO can be considered as such a metal. Recently, measurements have confirmed another such transport half-metal, namely CrO_2 ([Ji01] extracted $P_{Nv} = 0.96$).

Mazin describes various other definitions for DSP, valid for transport measurements in tunnel junctions, diffusive contacts (contacts with a large dimension compared to the mean free path) and ballistic contacts with an extremely high chance of reflection at the interface. However, no further attention to these definitions will be given here.

2.2 Contacts in the ballistic and diffusive regime

The ballistic and diffusive regime

Contacts between two materials can exist in various different shapes and sizes. To simplify the situation, a contact is represented by two reservoirs connected by a short link with radius a, as sketched in Figure 8. This a is referred to as the contact radius. Important for the transport of electrons through the link is the mean free path l of the electrons (l represents the average distance an electron can travel without colliding). The ratio a/l basically determines the physics behind the transport. Two limits for this ratio are

$$\text{diffusive regime: } \frac{a}{l} \gg 1, \qquad \text{ballistic regime: } \frac{a}{l} \ll 1. \tag{6}$$

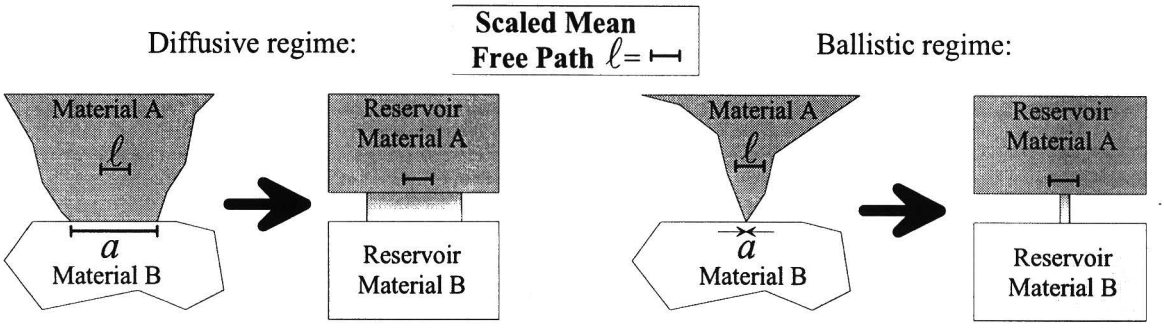

Figure 8: Schematic representation of contacts by connecting reservoirs. Transport through a contact can be characterized by the ratio a/l.

Regarding the contact itself, one may note that in the diffusive regime the electron transport is ruled by collisions while these effects are no longer dominating in the ballistic regime. For various metals (Nb, Au, Pb and Co), l is on the order of 100 Å at liquid ^{4}He-temperatures and strongly depends on temperature, purity, crystal structure and other material properties [Bass82].

Generally, it is not straightforward to give an analytical expression for the resistance of a contact. Scattering between electrons moving through the contact complicates the use of a simplified approach. However, contacts in the ballistic regime are so small that the electron-electron scattering is neglected. In this case, the resistance is given by (ρl) divided by the contact size, with ρ representing the electrical resistivity. This approach was worked out by Sharvin [Sha65] and therefore its resistance is referred to as the Sharvin resistance R_{sh}, given by

$$R_{sh} = \frac{4}{3}\frac{\rho l}{\pi a^2}. \tag{7}$$

The factor of $\frac{4}{3}$ comes from integration over all angles. Since ρl is approximately temperature independent with $\rho l \simeq 1$ fΩ·m^2 [Bass82] (or $a\sqrt{R}$=20 nm$\sqrt{\Omega}$), the resistance varies only with contact radius. Typically, ballistic point contacts have a (Sharvin) resistance in the range of 1 Ω-50 kΩ, where the upperbound corresponds roughly to the resistance of a single-atom contact ($a \simeq 1$ Å).

The resistance R_N for contacts not in the ballistic regime but in the quasi-ballistic regime ($a \approx l$), is given by the diffusive Maxwell correction to R_{sh} [Jan89], of which an approximation results in

$$R_N = R_{sh}\left(1 + \frac{a}{l}\right). \tag{8}$$

Motivation for measuring in the ballistic regime

In an attempt to model conductance through contacts, the assumption of a ballistic contact allows a relatively simple approach. One reason for this lies is the fact that in the ballistic regime, one can assume an abrupt drop in the voltage at the interface while in the diffusive regime one has to calculate the decrease by solving self-consistently the appropriate

transport equations.

Additional complications arise in a nonballistic contact between a normal metal and a superconductor. Increasing the contact size a will shift the regime from the ballistic regime, via the so-called mesoscopic regime towards the diffusive regime $a \gg l$. Already in this mesoscopic regime complex physical effects enter the picture. Zero-bias and above-gap conductance anomalies are examples of measured effects [Xio93, Kim00]. It is believed that these effects originate from quantum interference and other phase-coherent effects [Been97].

Interfacial scattering in the ballistic regime

Another insurmountable aspect of a contact is the fact that a perfectly clean contact is not achievable. Lattice distortions, oxide layers and surface effects will always be present and will influence the conductance. One way to take elastic scattering into account is the introduction of a potential barrier in the form of a δ-function. This barrier $V(x)$ is present at the interface between the two contacting materials and is formulated as

$$V(x) = W \cdot \delta(x). \tag{9}$$

The factor W (with dimension [J·m]) is referred to as the barrier strength. Standard quantum mechanics can be applied to calculate the probability $R(E_F)$ that an electron with energy E_F is reflected at the barrier, automatically leading to the probability of transmission $T(E_F)$ since $R + T = 1$. Calculations [Gri95] show that

$$T(E_F) = \frac{1}{1 + \frac{k_F^2 W^2}{4E_F^2}}, \qquad R = 1 - T. \tag{10}$$

Since these probabilities play a major role in transport through the contacts, Equation 10 is written in a more convenient form through normalization of W, given by

$$Z = \frac{k_F W}{2E_F} : \qquad T(E_F) = \frac{1}{1 + Z^2}, \quad R(E_F) = \frac{Z^2}{1 + Z^2}. \tag{11}$$

The parameter Z is dimensionless. For nonzero Z-values, a part of incoming electrons will reflect back resulting in an increase of the resistance to R_Z. It can be shown that, see Section 3.2, R_Z for a ballistic contact is given by

$$R_Z = R_{sh}\left(1 + Z^2\right). \tag{12}$$

Even in extremely clean contacts, interfacial scattering can occur due to the mismatch of the Fermi velocities of the two materials A and B. The Fermi mismatch is symbolized by the ratio r, given by $r = \frac{v_{F,A}}{v_{F,B}}$. It can be incorporated into an effective Z_{eff}, which is now a sum of the contribution given by Equation 9 and the Fermi mismatch contribution [Blo83]. This results in

$$Z_{eff}^2 = \frac{(1 - r)^2}{4r} + Z^2. \tag{13}$$

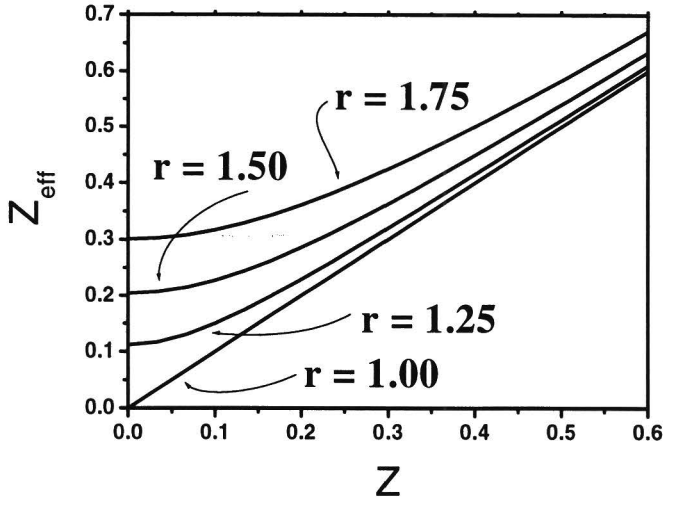

Figure 9: Existence of a Fermi velocity mismatch ($r = v_{F,A}/v_{F,B}$) results in a higher effective scattering parameter Z_{eff} .

The plot in Figure 9 shows the behaviour of Z_{eff} versus Z for various ratio's r. It should be noted that the result for Z_{eff} is the same if the Fermi velocities are interchanged. In the remaining part of this report the parameter Z_{eff} is shortened to Z.

2.3 Introduction to superconductivity

This section will introduce the basics of various superconducting properties, based on the BCS theory [BCS57]. This microscopic theory of superconductivity is an extension to earlier work done by Fröhlich [Frö50] and Cooper [Coo56]. An introduction on a sophomoric level to this work can be found in [Ros78].

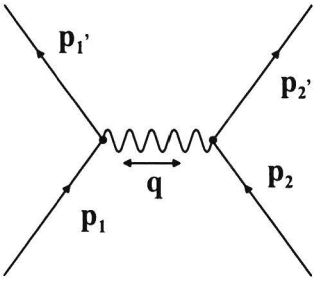

Figure 10: Schematic representation of electron-electron interaction through successive emission and absorption of a phonon.

The Cooper pair

In a normal metal at T=0, all electron states up to ϵ_F are filled, and the ensemble of these states is referred to as the Fermi sea. In 1956 Cooper presented the basic idea that a weak attractive interaction can bind pairs of electrons into a bound state in a superconductor. Cooper showed that, regardless of how weak the interaction is (as long as it is attractive), there are always some electrons within this sea that are unstable against the formation of at least one bound pair. Fröhlich's phonon-induced electron-electron interaction (see Figure 10) is considered to be the responsible interaction. It is based on successive phonon-emission by one electron (momentum p_1) and phonon-absorption by the second one (momentum p_2), with q the phonon momentum. One can compare this attractive interaction with the attractive Coulomb interaction, realized through successive emission and absorption of a photon.

In Cooper's result, the role of the background of the Fermi sea is crucial. Consider the two electrons that form a bound state. The two electrons interact with each other (Fröhlich's interaction) but not with those in the Fermi sea, except via the exclusion principle. Fröhlich derived that the state of lowest energy is formed, if the two considered electrons have equal but opposite momenta. In analogy to the hydrogen molecule, the strongest interaction is obtained with the electron spins opposite. Therefore, the pair can be written as a superposition of two-electronic states with equal and opposite momenta. From a temporal viewpoint, this superposition if translated to a continuous changing (or scattering) of the two-electron momentum combination $(p_{i\uparrow}, p_{i\downarrow})$ to $(p_{j\uparrow}, p_{j\downarrow})$. Since Fröhlich's interaction is attractive, $p_j > p_i$ and/or $p_j > p_F$ are energetically allowed, providing that $2(\epsilon_j - \epsilon_i)$ does not exceed the attractive potential.

It may also be clear, why the Fermi sea is of crucial importance via the exclusion principle: in order to perform continuous scattering to other $(p_{j\uparrow}, p_{j\downarrow})$-states, these states have to be vacant first.

BCS theory

Bardeen, Cooper and Schrieffer were the first to treat all electrons from a similar point of view. This leads to a more realistic expression for the superconducting ground state. They made use of a representation of the ground state in terms of electron creation operators, operating on the vacuum state with no electrons. Again, one makes use of the simplifying assumption that the matrix element $V_{i'i}$=$\langle p_{i'}, -p_{i'}|V|p_i, -p_i\rangle$ of the phonon-induced electron-electron interaction is given by

$$V_{i'i} = \begin{cases} -V & \text{if } |\epsilon_{i'} - \epsilon_F| \leq h\upsilon_L \text{ and } |\epsilon_i - \epsilon_F| \leq h\upsilon_L \\ 0 & \text{otherwise,} \end{cases} \tag{14}$$

with $h\upsilon_L$ the 'average' phonon energy ($h\upsilon_L \ll \epsilon_F$) and h Planck's constant. Applying a variational method, they obtained a solution for the ground state of the superconductor. One of the results that one can calculate from this, is the probability $|h_i|^2$ that the single-electron states $(p_{i\uparrow}, -p_{i\downarrow})$ are occupied at T=0. This function is plotted in Figure 11 and

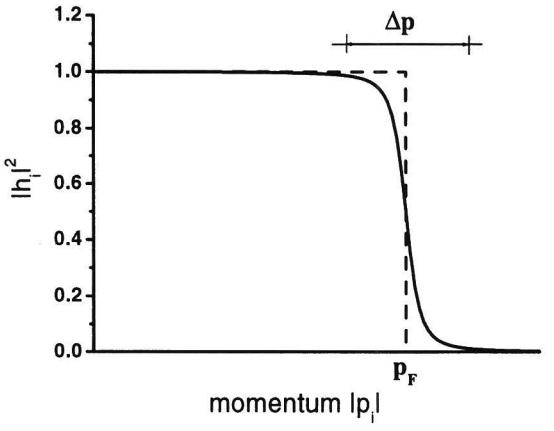

Figure 11: The dashed line represents the probability $|h_i|^2$ that (at absolute zero) the single-electron states $(p_{i\uparrow}, -p_{i\downarrow})$ are occupied in a normal metal. The same probability for state-occupation is shown for a superconductor, where even at $T = 0$ several states with $|p_i| > p_F$ can be occupied.

is given by

$$h_i = \frac{1}{2}\left[1 - \frac{\epsilon_i - \epsilon_F}{\sqrt{(\epsilon_i - \epsilon_F)^2 + \Delta^2}}\right], \tag{15}$$

with $\epsilon = p^2/2m$. The quantity Δ, which has the dimensions of energy, turns out to be of fundamental importance and is given by

$$\Delta_{T=0} = 2h\upsilon_L \exp\left[-\frac{1}{N(\epsilon_F)V}\right], \tag{16}$$

with $N(\epsilon_F)$ the density of states at the Fermi energy. Typical values for Δ and ϵ_F are 1 meV and 5 eV respectively.

One might wonder why not all electrons form Cooper pairs. In order for a non-interacting electron pair $(p_{i,\uparrow}, -p_{i,\downarrow})$ (with $p_i < p_F$) to form a Cooper pair, the individual energy of each electron must be raised to $\simeq \epsilon_F$ in order to experience nonzero attractive Fröhlich interaction (Equation 14). An energy benefit is only realized for those non-interacting pairs that satisfy $V > 2(\epsilon_F - \epsilon_i)$, which is similar to the demand $\epsilon_i > \epsilon_F - \frac{V}{2}$.

Excitations and quasi-particles

An important limitation of the BCS theory is its restriction to the ground state (also referred to as the condensate). Bogoliubov extended the approach in such a way that also excited states are described. This theory leads to essentially the same result for the ground state as previously derived, however in addition, it leads to the introduction of the concept of quasi particles. The following will clarify this concept.

If sufficient energy is imparted to the ground state (by heating, illumination, etc.), a Cooper pair may break up into two individual 'particles', which no longer have equal and opposite momenta p_i and p_j. These 'particles' behave almost like free electrons and are therefore referred to as quasi-particles. If the quasi-particle occupies a state that was previously empty, it is referred to as an electron-like quasi-particle (ELQ), with base state $|\text{e-like}\rangle$. However, if the quasi-particle occupies a state that was previously part of the Cooper-pair momentum domain, it is referred to as a hole-like quasi-particle (HLQ), with base state $|\text{h-like}\rangle$. The $|\text{e-like}\rangle$- and $|\text{h-like}\rangle$-states are two extremities. Generally, a quasi-particle will occupy a state that previously had a chance h_i (see Equation 11) of being occupied, and the quasi-particle state is a superposition of the $|\text{e-like}\rangle$-state and the $|\text{h-like}\rangle$-state. The wavefunction of a quasi-particle can be described by the wavefunction

$$\Psi(x,t) = f(x,t)|\text{e-like}\rangle + g(x,t)|\text{h-like}\rangle, \qquad \text{or} \quad \Psi(x,t) = \begin{pmatrix} f(x,t) \\ g(x,t) \end{pmatrix}. \tag{17}$$

The $|\text{e-like}\rangle$ quasi-particle obeys the Schrödinger equation,

$$i\hbar\frac{\partial f}{\partial t} = Hf \qquad \text{where} \quad H = -\frac{\hbar^2}{2m}\frac{d^2}{dx^2} - E_F + V(x), \tag{18}$$

while an $|\text{h-like}\rangle$ quasi-particle obeys the the time-reversed Schrödinger equation,

$$i\hbar\frac{\partial g}{\partial t} = -Hg. \tag{19}$$

The base states are coupled by the energy $\Delta(x)$ so that the wave-function Ψ obeys

$$i\hbar\frac{\partial \Psi}{\partial t} = \begin{pmatrix} H & \Delta \\ \Delta & -H \end{pmatrix}\Psi, \tag{20}$$

which is the Bogoliubov-de Gennes equation. Since the hamiltonian matrix is independent of time, the substitution $\Psi(x,t) = \psi(x)e^{-i\omega t}$, where $E = \hbar\omega$, reduces equation (20) to

$$\begin{pmatrix} H & \Delta \\ \Delta & -H \end{pmatrix}\psi = E\psi. \tag{21}$$

A first assumption is made by setting $V(x) = 0$. A second assumption is that Δ is independent of position x. These two assumptions allow analytical evaluation of Equation 21. This approximation is referred to as the 'free quasi-particle approximation'. For the trial solution

$$\psi = \begin{pmatrix} u \\ v \end{pmatrix} e^{ikx} \tag{22}$$

one finds that

$$E^2 = \left(\frac{\hbar^2k^2}{2m} - E_F\right)^2 + \Delta^2. \tag{23}$$

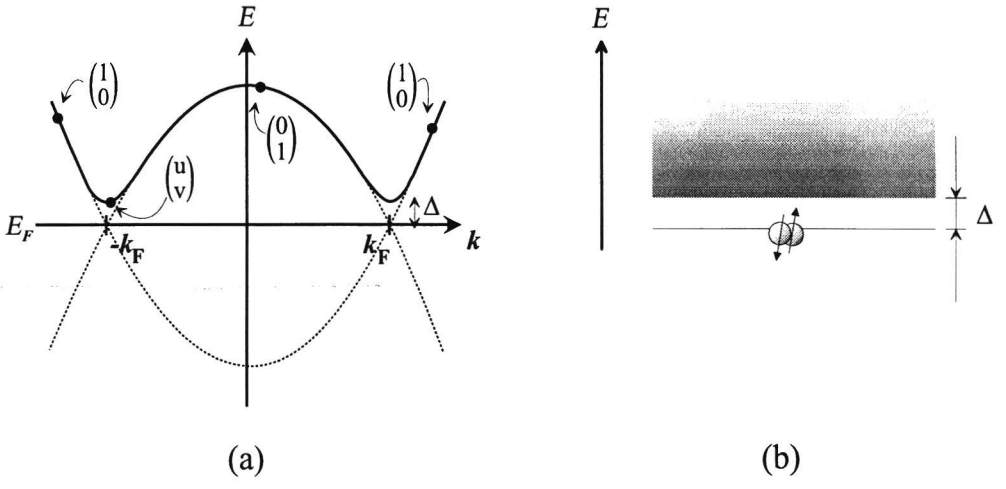

Figure 12: (a) Excitation energy of the quasi-particles as a function of k. (b) At T >0, the quasi-particles have a nonzero occupation probability, as displayed in the superconducting energy diagram.

Since one must impart energy to break up a Cooper pair, the quasi-particle energy E must have a positive value. Therefore, only the positive root of Equation 23 is taken. Due to the offset $-E_F$, the energy is measured from the Fermi-level and is therefore referred to as the excitation energy of the quasi-particle. Figure 12-(a) shows E as a function of k, where it is indicated (dashed lines) how the curve is composed of the two functions which represent the positive and negative root of E^2 (Equation 23) at Δ=0. To illuminate the parameters u and v, their values are given at various marked spots on the $E-k$ curve. The minimal energy required to break up a pair is given by 2Δ, with Δ introduced by Equation 16. The quantity Δ is also referred to as the superconducting bandgap. The energy diagram for the superconductor at temperature $T > 0$ is represented by Figure 12-(b).

As the temperature is raised, more and more Cooper pairs are split up, accompanied by a lowering of Δ (see Figure 13). Eventually at a critical temperature T_c, no Cooper pairs have remained, Δ has reduced to zero, and the quasi-particle states are identical to electron states in a normal metal.

An energy representation for all unpaired electrons

Consider a normal metal at $T = 0$, see Figures 14-(a) and 14-(b). In the electron band, all states up to E_F are filled (represented by •), while the states $E > E_F$ are not occupied, leaving a hole behind (represented by ○). By considering the hole as a particle obeying Equation 19, one has defined the 'hole-like particle'. The middle image shows the energy band for such particles as well as its occupied states at T=0, where • represents an occupied hole-like state and ○ a vacant hole-like state. From this point of view, the occupied X-state in 14-(a) is equivalent to the vacant Y-state in 14-(b) (with $E_X = -E_Y$ and $k_X = -k_Y$).

A similar approach can be made for all unpaired electrons in the superconductor. Since at $T = 0$ all quasi-particle states are vacant, the energy states at $-E$ must be occupied.

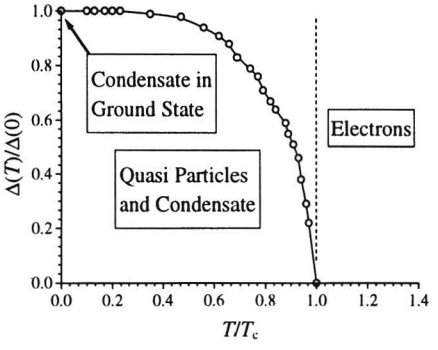

Figure 13: Temperature dependence of the superconducting bandgap Δ. At $T > T_c$ all Cooper pairs are split up and superconductivity no longer exists.

Such an argument results in the two mirrored $E - k$ curves in Figure 14. It is emphasized one more time, that the states at $E < 0$ do not represent quasi-particle states. The 'particles' with $E < 0$ behave as normal electrons for $|k| \ll k_F$, while for $|k| \gg k_F$ they act as hole-like particles. One could have derived the same diagram in the figure at once, if also the negative root of equation 23 was considered.

The superconducting density of states

Equation 23 can also be used to determine the superconducting density of states $N(E)$, defined as $N(E) = dN/dE$. Note that $N(E)$ also considers electron states with $E < 0$. One can derive that $N(E) = \frac{dN}{d\varepsilon}\frac{d\varepsilon}{dE}$ with $\frac{dE}{d\varepsilon}$ given by

$$\frac{dE}{d\varepsilon} = \frac{\varepsilon}{\sqrt{\varepsilon^2 + \Delta^2}} = \frac{\sqrt{E^2 - \Delta^2}}{|E|}, \tag{24}$$

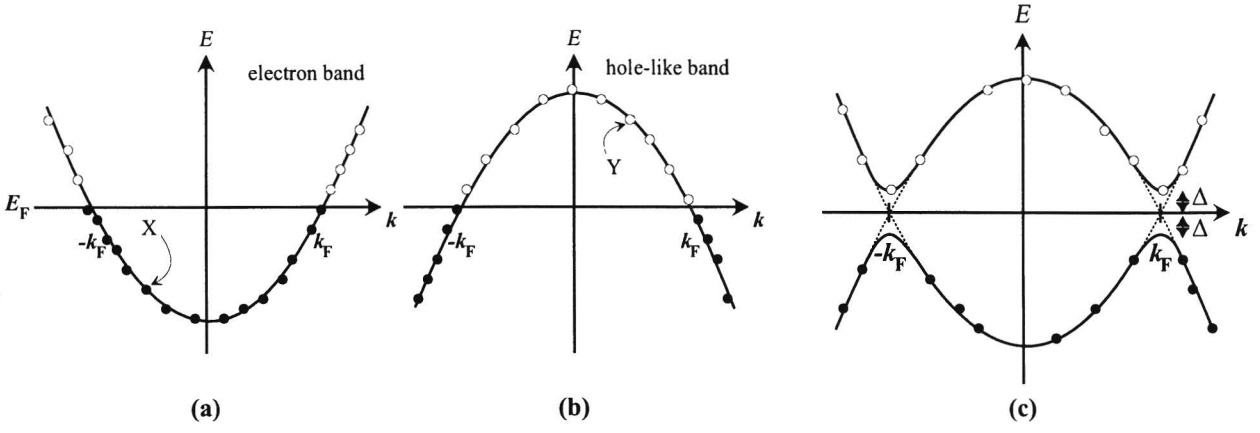

Figure 14: For a normal metal at T=0, the occupied states (•) in the electron and hole-like band are shown in (a) and (b). The occupation of the $E - k$ bands for a superconductor at $T = 0$ is plotted in (c).

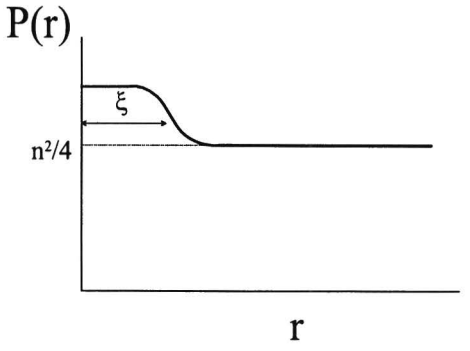

Figure 15: The probability $P(r)d\tau_1 d\tau_2$ of finding an electron $p_\uparrow$ in a volume element $d\tau_2$ at a distance r from a volume element $d\tau_1$ which contains an electron $-p_\downarrow$.

and ε defined as $\frac{\hbar^2 k^2}{2m} - E_F$. Note that $\frac{dN}{d\varepsilon}$ is the DOS for electrons in a normal metal. By assuming a constant value for $\frac{dN}{d\varepsilon} = N_0$, which is valid for small E, one can retrieve

$$N(E) = \begin{cases} 0 & \text{for } |E| < \Delta \\ N_0 \frac{|E|}{\sqrt{E^2 - \Delta^2}} & \text{for } |E| \geq \Delta. \end{cases} \tag{25}$$

Space correlations: the coherence length

After evaluating the Cooper pair from an energy-point of view, one might wonder how one can spatially characterize the Cooper pair. One way to express the spatial behaviour is by calculating the probability $P(r)d\tau_1 d\tau_2$ of finding an electron $p_\uparrow$ in a volume element $d\tau_2$ at a distance r from a volume element $d\tau_1$ which contains an electron $-p_\downarrow$. If there are no correlations (e.g. in a normal metal) this probability is given by $\frac{1}{4}n^2 d\tau_1 d\tau_2$, with n the total number of electrons. Detailed calculations for a superconductor show that the continuously mixing of the momentum states results in a raising of the chance $P(r)d\tau_1 d\tau_2$ for small values of r. This is indicated in Figure 15. The length of the raised-$P(r)$ region is referred to as the (Pippard) coherence length ξ. The coherence length represent the dimension of one Cooper pair, which is on the order of 10-1000 nm. Notice that the volume ξ^3 contains the centers of mass of about 10^7 other pairs, so that the pair wave functions overlap considerably.

The critical temperature and field

Figure 13 shows how an increase in temperature can eventually destroy superconductivity. The value for T at which this occurs is referred to as the critical temperature T_c. Superconductivity can also be destroyed if a sufficiently high magnetic field is applied, referred to as the critical field H_c. Generally, H_c will decrease as a function of increasing temperature to eventually $H_c = 0$ at $T = T_c$.

The previous is true for type-I superconductors. Type-II superconductors are generally characterized by two critical fields, namely $H_{c1}(T)$ and $H_{c2}(T)$ ($H_{c1} < H_{c2}$). If the field

H_{c1} is applied to a type-II superconductor, the destruction of superconductivity is initiated but only completed at an applied field H_{c2}. In the following, the critical field H_{c1} for a type-II superconductor is represented by H_c.

2.4 Destruction of superconductivity in conductance measurements

A current I through the superconducting tip will generate a magnetic field. If the current reaches the critical value I_c, the generated field equals H_c and superconductivity is (partially) destroyed. The voltage at which the critical current I_c is generated is referred to as V_c.

Consider a superconducting wire of radius a, carrying the current I. The field H generated at the perimeter of the wire is given by

$$H = \frac{I}{2\pi a}. \tag{26}$$

One can, in good approximation, use Equation 26 to calculate the magnetic field present at the perimeter of the sample/tip contact. The question now is, whether the radius a of the contact is of a sufficiently small order of magnitude to yield $H \simeq H_c$.

The typical resistance of a contact is 10 Ω, see Section 2.2. For such a contact one can expect a contact size of circa 10 nm. The applied voltage will be on the same order of magnitude as the superconducting bandgap, which is $\approx$1 meV, resulting in a current on the order of 0.1 mA. Use of Equation 26 gives a generated field of several kA/m. Although the critical field for small specimens in proximity of a normal metal is not known, bulk values for various superconductors are of comparable magnitude. Therefore, it may be possible that a conductance measurement indicates partial destruction of superconductivity, as explained below.

The Westbrook-Javan model

A model posed by Westbrook and Javan [West99] predicts the voltage V_c at which one can observe partial destruction of superconductivity.

Figure 16 shows typical current I- and conductance $G = dI/dV$-curves for (a) an N/N contact, (b) an N/S contact and (c) an N/S contact with destruction of superconductivity at $|V| > V_c$. The current $I_{NS}(V)$ through an N/S contact can be described by $I_{NS} = I_{NN} + I_{exc}(V)$, that is, when one switches from the N/S state to the N/S state the current is raised by $I_{exc}(V)$ due to Andreev Reflection. The current $I_{exc}(V)$ is referred to as the excess current. In Figure 16, the function I_{exc} has a constant value $I_{exc}(\Delta)$ for $\Delta < |V| < V_c$. At V_c superconductivity is partially destroyed and I_{exc} will drop to a lower value. For clarity, in the figure the superconductivity is completely destroyed at V_c. The drop of I_{exc} is seen as a peak in the conductance curve depending of the 'sharpness' of the transition. Westbrook and Javan were able to measure such peaks, of which several (differential resistance) dV/dI-curves are shown in Figure 17 (left).

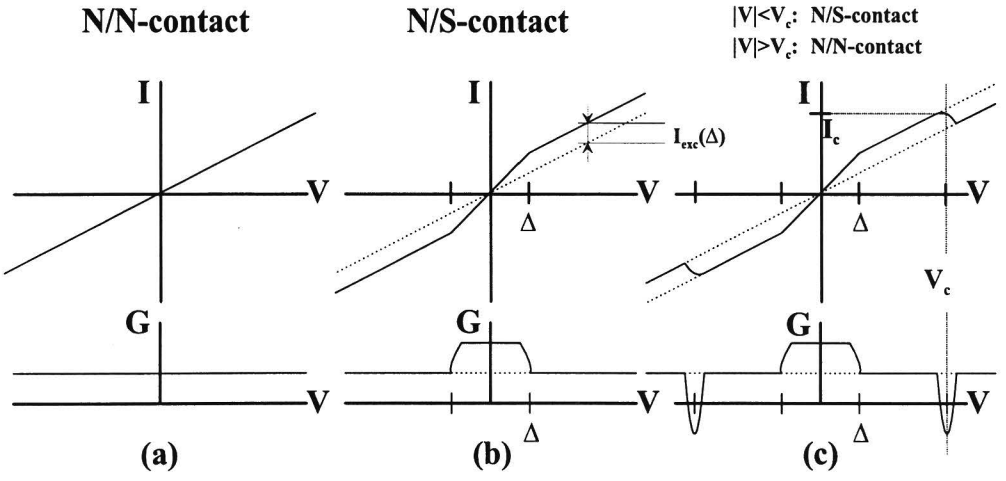

Figure 16: The $I-V$ curves and $G-V$ curves for (a) an N/N contact, (b) an N/S contact and (c) an N/S contact with destruction of superconductivity at $|V| > V_c$.

From now on, only voltages $V > \Delta$ are considered. The current I through an N/S contact consists of the two contributions

$$I(V > \Delta) = \frac{V}{R_N} + I_{exc}(\Delta), \tag{27}$$

with R_N the constant resistance of the contact at $V > \Delta$. In [BTK82] it is shown that $I_{exc}(\Delta) \sim \Delta$ and $I_{exc}(\Delta) \sim 1/R_N$, for constant Z. At $I{=}I_c$, Equation 27 reads $I_c = \frac{V_c}{R_N} + I_{exc}(\Delta)$. Combining this expression with Equation 26 one finds

$$V_c = (2\pi a H_c)R_N - I_{exc}(\Delta)R_N. \tag{28}$$

It has previously been discussed (Equation 7) that $a\sqrt{R_{sh}}$ is a constant (20 nm$\sqrt{\Omega}$), with R_{sh} the Sharvin resistance in the ballistic regime. Therefore, in the ballistic limit ($R_N = R_{sh}$), Equation 28 can be rewritten as

$$V_c = k\sqrt{R_N} + V_0, \quad \text{with} \quad k = 2\pi H_c\sqrt{R_{sh}a^2} \quad \text{and} \quad V_0 = -I_{exc}(\Delta)R_N. \tag{29}$$

In this formula V_0 has a negative value. However, the measurements which will be introduced in Section 5.5, as well as those performed by Westbrook and Javan, show a positive V_0. An extension of the model to the quasi-ballistic regime will account for this, as will be derived here. For such contacts, the diffusive Maxwell correction can be applied, as introduced by Equation 8. This expression is used to rewrite the term $a\sqrt{R_N}$ in Equation 28, resulting in

$$a\sqrt{R_N} = a\sqrt{R_{sh}(1+\frac{a}{l})} \simeq a\sqrt{R_{sh}} + \frac{a^2\sqrt{R_{sh}}}{2l}. \tag{30}$$

Also in this quasi-ballistic diffusive regime one can rewrite Equation 28 into the form $V_c = k\sqrt{R_N}+V_0$. Equation 30 is used to determine the constant k and V_0, now defined as

$$k = 2\pi H_c\sqrt{R_{sh}a^2} \quad \text{and} \quad V_0 = \frac{\pi H_c(R_{sh}a^2)}{l} - I_{exc}(\Delta)R_N. \tag{31}$$

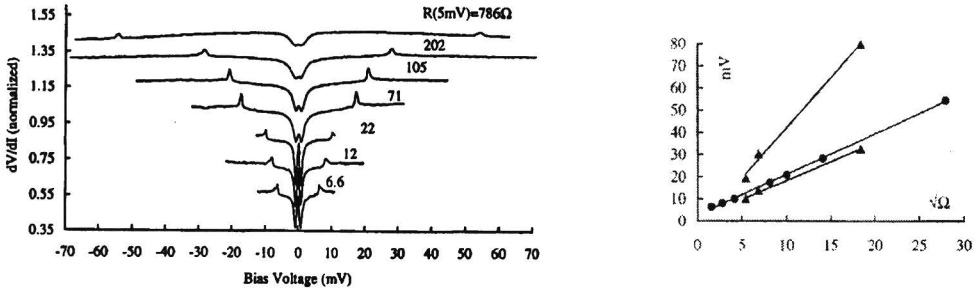

Figure 17: Measurements performed by Westbrook and Javan, showing peaks in the $dV/dI - V$ curves (left). The voltage V_c at which superconductivity is destroyed is linearly dependent on the square root of the resistance.

In the derivation of V_0 in Equation 31, the assumption $(1\text{-}\frac{a}{2l}) \simeq 1$ has been made. The values for V_c, measured by Westbrook and Javan, are plotted versus $\sqrt{R}$ in Figure 17 (right), confirming the linear dependency. More attention to both plots is given in Section 5.5.

2.5 Contacts on the order of the coherence length

So far, superconductivity was discussed for objects that are large compared to the coherence length ($\xi \simeq$10-1000 nm). However, since this report describes contacts in the ballistic or quasi-ballistic regime, the contact radius is on the order of ξ and locally (at the interface) one might expect a change in various superconducting properties.

One can represent the tip in the form of a cone, which is truncated at the position of the sample, see Figure 18. Following a 'geometrical' intuitive model, one can imagine that the Cooper pairs (characterized by the coherence length ξ) are hindered in entering the end of the tip and a position of maximal penetration exists. One can compare such a system to a superconductor in contact with a normal metal, where Levi *et al* [Levi98] observed that due to proximity effects, a nonzero value for the bandgap in the N-side was observed. They showed that this value decreases as a function of position from the interface, to eventually zero at a distance comparable to the superconducting coherence length. In analogy to their observations, the local bandgap at the end of a cone-shaped tip (position x) is also assumed to decay over a length scale of ξ. As a first guess, the following relation is assumed

$$\frac{\Delta(x)}{\Delta_0} = \exp -\frac{x}{\xi}, \tag{32}$$

with Δ_o the superconducting bandgap at $x < 0$. It should be noted that this particular tip geometry can result in a Δ_0 different from the bulk value Δ_{bulk}.

The contact is positioned at x, see Figure 18. With increasing x one can see that the contact radius decreases, until eventually the end of the tip is reached. To express x as

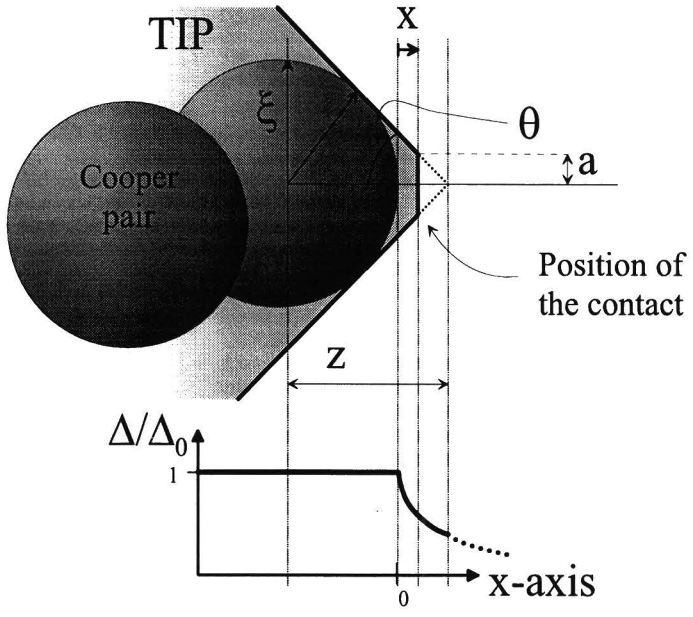

Figure 18: Representation of a Cooper pair (with characteristic length ξ), blocked by the geometry of the tip so that the tip's end is positioned 'outside' the pair. The bandgap Δ is assumed to decay exponentially.

function of a, ξ and θ, the dependencies

$$\tan\theta = \frac{a}{z - \xi - x}, \quad \text{and} \quad z = \frac{\xi}{\sin\theta} \tag{33}$$

lead to

$$x = \frac{\xi}{\sin\theta} - \xi - \frac{a}{\tan\theta}. \tag{34}$$

By substituting expression 34 for x, one can transform Equation 32 into

$$\frac{\Delta(a)}{\Delta_0} = \exp\left(1 - \frac{1}{\sin\theta}\right) \exp\frac{a}{\xi\tan\theta}. \tag{35}$$

By assuming a constant for $a\sqrt{R}$, which is valid in the ballistic regime (see Section 2.2), Δ as function of R can be formulated as

$$\Delta(R) = p_1 \exp\frac{1}{p_2\sqrt{R}}, \tag{36}$$

with

$$p_1 = \Delta_0 \exp\left(1 - \frac{1}{\sin\theta}\right), \quad \text{and} \quad p_2 = \frac{\xi\tan\theta}{a\sqrt{R}}. \tag{37}$$

In conclusion, this geometrical intuitive model results in an expression for the decay of the local bandgap versus resistance. The decay is influenced by the tip geometry θ, and by the superconducting properties ξ and Δ_0.

3 The original and modified Blonder-Tinkham-Klapwijk model

This chapter roughly follows the same outline as the theory described in [Kant00]. However, some subjects are discussed more extensively. First an intuitive model is given that can predict the basic characteristics of conductance curves for N/S contacts. The Blonder-Tinkham-Klawpijk model, which will be introduced in Section 3.2, treats the transport through an interface in more detail. It is based on the solutions to the BdG-equation (derived in the previous chapter) and is restricted to nonpolarized-N/S contacts. Therefore, also a modification to the BTK model is presented which does include spin polarization. The last section gives comments on N/S contacts with $\Delta \approx kT$ and with high-Z.

3.1 Andreev Reflection in clean contacts

One can understand the essence of the conductance behaviour through an N/S contact by comparing it to the constant conductance G_{NN} through an N/N contact.

Conductance through a nonpolarized-N/S contact

In the following intuitive approach, a perfectly clean interface (Z=0, see Section 2.2) is assumed. Consider the situation of a small applied voltage $eV \ll \Delta$, raising the energy of the electrons that contribute to the current to $E_F + eV$. The possibilities for such an electron are limited. It can not reflect back (since Z=0) and it can not enter the superconductor as a quasi-particle. Therefore, it is forced to take along a second electron and form a Cooper pair, resulting in a conductance that is twice as high as a for a contact consisting of two normal metals.

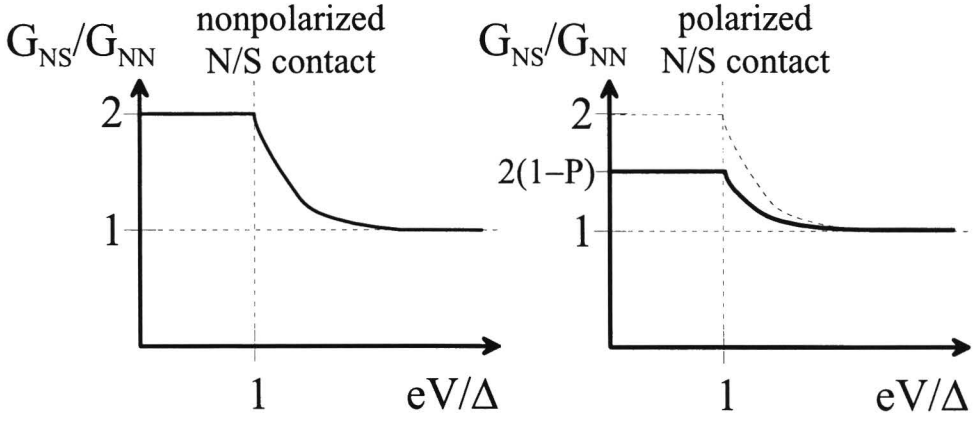

Figure 19: The normalized conductance (G_{NS}/G_{NN}) plotted for a clean nonpolarized-normal-metal/superconductor and for a clean polarized-normal-metal/superconductor contact. At $V = 0$, the normalized conductance is given by $2(1 - P)$.

At voltages $eV \gg \Delta$, the electron has the possibility to enter the superconductor as a quasi-particle. Its energy is so large compared to the bandgap, that the influence of Δ is negligible in that the available quasi-particle state does not differ from the electron state. In other words, there is no reason for the electron to combine with a second electron and form a Cooper pair. Therefore, the conductance at high voltages is the same as the conductance through an N/N contact. The behaviour of G_{NS} versus eV is sketched in the left image of Figure 19.

Conductance through a polarized-N/S contact

Consider a polarized metal of which its current I is carried by spin-up electrons ($I_\uparrow$) and spin-down electrons ($I_\downarrow$). The spin polarization of this current is defined as $P = |I_\uparrow - I_\downarrow|/(I_\uparrow + I_\downarrow)$, and for simplicity, $I_\uparrow > I_\downarrow$ is defined. The behaviour of the electrons at $eV \gg \Delta$ is identical to the situation of a nonpolarized-N/S contact. However, at $eV \ll \Delta$ the chance for Cooper-pair formation is reduced by a factor (1-P), since only $I_\downarrow$ can be doubled through Cooper-pair formation, preventing $I_\uparrow - I_\downarrow = PI$ from further current contribution. The resulting normalized conductance is now given by

$$\frac{G_{NS}}{G_{NN}} = 2(1-P), \qquad \text{at} \quad eV \ll \Delta. \tag{38}$$

This reduction of the conductance is plotted in the right image of Figure 19.

3.2 The BTK model excluding spin polarization

The BTK model, named after Blonder, Tinkham and Klapwijk [BTK82], calculates the current (and conductance) through a ballistic contact between a nonpolarized normal metal N and a superconductor S. The principles of the model can be better understood if one places the energy diagrams of a normal metal and a superconductor (introduced in Section 2.3) next to each other, as done in Figure 20. Also for the normal metal, both the bands for the electrons and hole-like particles are displayed. A note should be placed at the fact that the BTK model assumes an abrupt increase of the bandgap from 0 in N to Δ in S.

Scattering probabilities for an electron at the N/S interface

Consider an electron, moving to the right in the normal metal, that has reached the interface. The electron has energy (E_F+E), wavevector (k_F+k_N), and is pointed out in the figure by '1'. At the interface, the electron can reflect as a hole (in order to from a Cooper pair in S) on the other side of the Fermi surface ($-k_F + k_N$) with probability amplitude a, reflect back into the normal metal -(k_F+k_N) with probability amplitude b, and transmit as a quasi-particle in the superconductor in two ways (k_F+k_S and $-k_F+k_S$), with probability amplitudes c and d. As discussed in Section 2.3, the reflected hole (amplitude a, energy $-E$ and $k = -k_F + k_N$) can also be displayed as an occupied hole-like state (amplitude a, energy E and $k = k_F - k_N$).

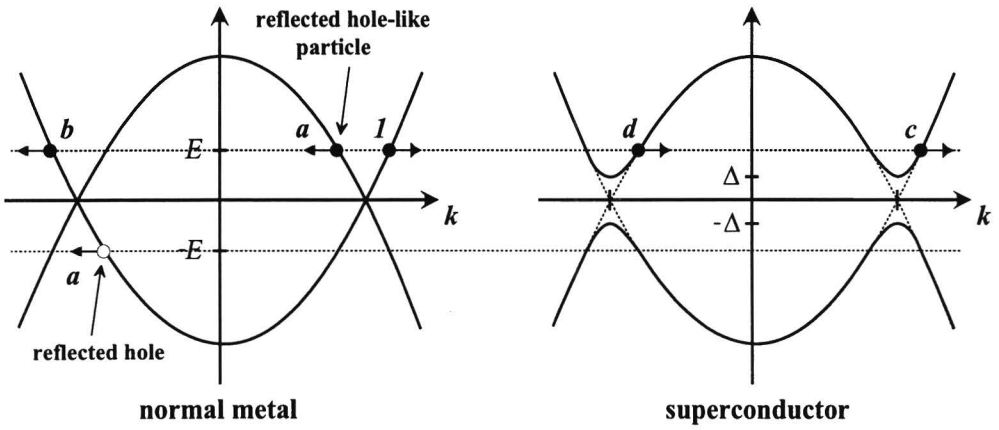

Figure 20: Energy diagram for (a) a normal metal (with $\Delta = 0$) and for (b) a superconductor with a finite Δ, showing the allowed horizontal transitions for an incoming electron, marked '1'.

In the normal metal, the solution of Equation 20 will have the form

$$\psi_N(x) = 1 \begin{pmatrix} 1 \\ 0 \end{pmatrix} e^{i(k_F+k_N)x} + a \begin{pmatrix} 0 \\ 1 \end{pmatrix} e^{i(k_F-k_N)x} + b \begin{pmatrix} 1 \\ 0 \end{pmatrix} e^{-i(k_F+k_N)x}. \tag{39}$$

In the superconductor, the solution of Equation 20 will be of the form

$$\psi_S(x) = c \begin{pmatrix} u \\ v \end{pmatrix} e^{i(k_F+k_S)x} + d \begin{pmatrix} v \\ u \end{pmatrix} e^{i(-k_F+k_S)x}, \tag{40}$$

Since both k_N as k_S are small compared to k_F, all powers of e in equations 39 and 40 can be replaced by e^{ik_Fx}. At this point the mechanism for reflection enters the picture (introduced in Section 2.2). In this section, an interfacial barrier was defined in the form of a delta-function $V(x) = W\delta(x)$, with the dimensionless normalized strength $Z = \frac{k_F W}{2E_F}$. The interfacial scattering enters the BdG-equation via the boundary conditions. As required by standard boundary conditions [Gri95], the wavefunction is continuous

$$\psi_N(0) = \psi_S(0) \equiv \psi(0) \tag{41}$$

and its derivative obeys

$$\psi'_S(0) - \psi'_N(0) = W\frac{2m}{\hbar^2}\psi(0), \tag{42}$$

as is appropriate for a δ-function potential with strength W. Equation 21 and the boundary conditions allow to solve for a, b, c and d.

The probability A for Andreev reflection and the probability B for normal reflection are equal to $|a|^2$ and $|b|^2$ respectively. The probability $C + D$ for transmission as a quasi-particle equals $1 - (A + B)$ since $A + B + C + D$=1. Figure 21 displays the probabilities A and B for different Z-values, for which the formulas are given in Table 1.

$\gamma^2 = [u_0^2 + Z^2(u_0^2 - v_0^2)]^2$
$u_0^2 = 1 - v_0^2 = \frac{1}{2}[1 + \sqrt{(E^2 - \Delta^2)/E^2}]$

	A(E)	B(E)
General form		
$E < \Delta$	$\frac{\Delta^2}{E^2+(\Delta^2-E^2)(1+2Z^2)^2}$	$1 - A(E)$
$E > \Delta$	$\frac{u_0^2 v_0^2}{\gamma^2}$	$\frac{(u_0^2-v_0^2)^2 Z^2(1+Z^2)}{\gamma^2}$
Strong barrier ($Z \gg 1$)		
$E < \Delta$	$\frac{\Delta^2}{4Z^4(\Delta^2-E^2)}$	$1 - A(E)$
$E > \Delta$	$\frac{u_0^2 v_0^2}{Z^4(u_0^2-v_0^2)^2}$	$1 - \frac{1}{Z^2(u_0^2-v_0^2)}$
N/N-contact ($\Delta = 0$)	0	$\frac{Z^2}{1+Z^2}$

Table 1: Calculated probabilities $A(E)$ and $B(E)$ for an N/S contact in general, an N/S contact with high Z and an N/N contact.

Calculation of the normalized conductance

The current through the N/S contact can be calculated either in the normal metal or in the superconductor. The first option is chosen for convenience. Figure 22 summarizes the energetically allowed scattering processes for an incoming electron. The factor X represents the contribution of scattering processes in the superconductor.

First the situation is considered at which no voltage difference over the contact is applied. Focusing only at the electron movement on the N-side, one can conclude that the current contribution $\mathrm{d}I_{N,N\rightarrow S}$ of electrons with energy $[E, E + \mathrm{d}E]$, moving from the normal metal to the superconductor, is equal to

$$\mathrm{d}I_{N,N\rightarrow S} = e\mathcal{A}v(E)N(E)[1 + A(E) - B(E)]f(E)\mathrm{d}E, \tag{43}$$

with e the electron charge, $v(E)$ the electron velocity, $N(E)$ the density of states, $\mathcal{A}$ the contact area and $f(E)$ the Fermi-Dirac distribution. Note that the Andreev-reflected hole has a positive contribution to the current.

Electrons which performed a transition from the superconductor into the normal metal also contribute to the N-current. Their contribution is

$$\mathrm{d}I_{N,N\leftarrow S} = -e\mathcal{A}v(E)N(E)X(E)\mathrm{d}E. \tag{44}$$

Since the net current $\mathrm{d}I_N(E) = \mathrm{d}I_{N,N\rightarrow S}(E) + \mathrm{d}I_{N,N\leftarrow S}(E)$ equals zero if no voltage is applied, one can derive that $X(E) = [1 + A(E) - B(E)]$.

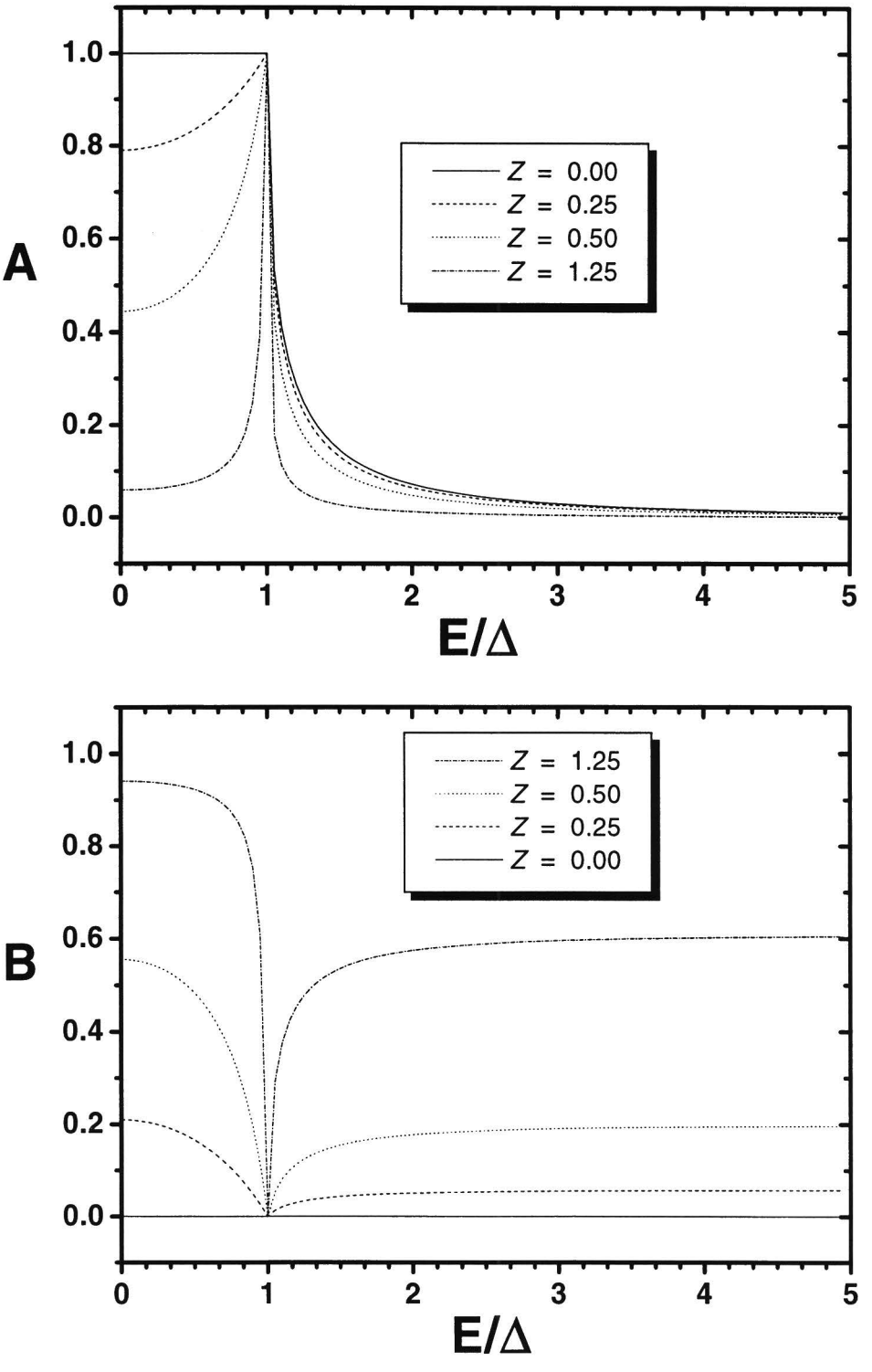

Figure 21: Probability for Andreev reflection (top) and for normal reflection (bottom) for various values of the elastic scattering parameter Z.

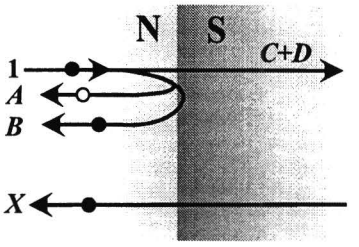

Figure 22: Illustration of the currents flowing in the normal-metal side of the contact.

In case of a finite voltage eV, a net current will flow. Suppose that the normal metal is raised in energy by eV. Section 2.2 discussed that, assuming a ballistic contact, one can simply replace $f(E)$ in Equation 43 by $f(E - eV)$. The net current in the N-side is now given by

$$\begin{aligned} \mathrm{d}I_N &= I_{N,N\to S}(E) + I_{N,S\to N}(E) = \\ &= e\mathcal{A}v(E)N(E)[1 + A(E) - B(E)][f(E - eV) - f(E)]\mathrm{d}E. \end{aligned} \tag{45}$$

The total current is obtained by integrating $\mathrm{d}I_N(E)$ over all energies, resulting in

$$I_N = e\mathcal{A}\int_E v(E)N(E)[1 + A(E) - B(E)][f(E - eV) - f(E)]\mathrm{d}E. \tag{46}$$

Since the function $[f(E - eV) - f(E)]$ is nonzero only in a small region around E_F, in which the velocity and density of states can be regarded as constants, one can extract $N(E_F) = N_0$ and $v(E_F) = v_F$ out of the integral.

The conductance $G_{NS} = dI/dV$ is given by

$$G_{NS} = -e^2\mathcal{A}v_F N_0 \int_E [1 + A(E) - B(E)]f'(E - eV)\mathrm{d}E. \tag{47}$$

One can evaluate the same expression in case of a contact between two normal metals (N/N-contact). In this case Δ=0 and Table 1 shows that $A(E)$=0 and $B(E) = 1/(1+Z^2)$. Equation 47 now reduces to

$$G_{NN} = -e^2\mathcal{A}v_F N_0 \frac{1}{1+Z^2}. \tag{48}$$

It is popular to normalize the conductance G_{NS} by the constant G_{NN}. G_{NN} can experimentally be deduced from measurements on N/S contacts since $G_{NN} = G_{NS}(V \gg \Delta)$. The formula for the normalized conductance is given by

$$\frac{G_{NS}(V)}{G_{NN}} = \frac{G_{NS}(V)}{G_{NS}(V \gg \Delta)} = -(1 + Z^2)\int_E [1 + A(E) - B(E)]f'(E - eV)\mathrm{d}E. \tag{49}$$

One can interpret the formula for the normalized conductance as that the function $[1 + A(E) - B(E)]$ is probed at $E = eV$ by the δ-function-like f', with varying eV. This is sketched in Figure 23.

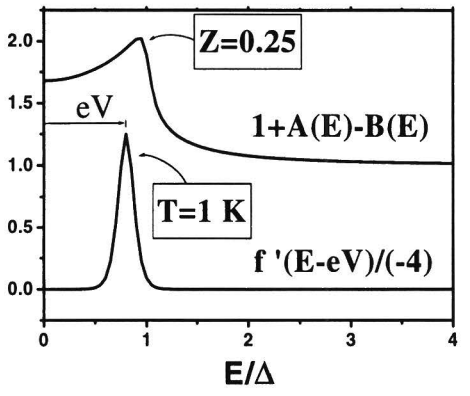

Figure 23: Illustration of the functions $[1 + A(E) - B(E)]$ (with Z=0.25) and $f'(E - eV)$ (normalized by factor -4) at T=1 K and V=0.8Δ.

Various conductance-versus-voltage curves are displayed in Figure 24, at the two temperatures 4.2 K and 1.5 K. Features around $V \simeq \Delta$ are, as expected, thermally smeared at 4.2 K with respect to the same features at 1.4 K. The introduction of Z seems to only decrease the normalized conductance at $V < \Delta$, and not at the regions $V \simeq \Delta$ (this is most clearly visible at 1.4 K). This results in the creation of two maxima and one minimum.

High-Z conductance curves

Table 1 displays the probabilities $A(E)$ and $B(E)$ for an N/S contact for high $Z \gg 1$. It follows that for such contacts, the electrons have a probability of almost 1 to reflect back into the metal, as expected. However, still a nonzero factor $[1 + A(E) - B(E)]$ will contribute to a net current towards the superconductor. At $|E| < \Delta$, $[1 + A - B]$=0, but at $|E| > \Delta$ this factor is given by

$$1 + A(E) - B(E) \simeq \frac{1}{Z^2} \frac{1}{u_0^2 - v_0^2} = \frac{1}{Z^2} \frac{|E|}{\sqrt{E^2 - \Delta^2}}. \tag{50}$$

One can see that the obtained formula for $[1+A-B]$ is proportional to the superconducting density of states $N_S(E)$, since the latter is given by Equation 25, namely

$$N_S(E) \sim \frac{|E|}{\sqrt{E^2 - \Delta^2}}, \qquad |E| \geq \Delta, \tag{51}$$

and $N_S(E) = 0$ for $|E| < \Delta$. Therefore, in the high-Z regime, Equation 47 can be rewritten as

$$G_{NS} \sim \int_E N_S(E) f'(E - eV) \mathrm{d}E. \tag{52}$$

This result is identical to conductance curves through an N/I/S tunnel junction, for which a phenomenological theory [Bar61] derives the same conductance behaviour as Equation 52. Therefore, one can also use the term 'tunnel regime' for a point contact with high Z.

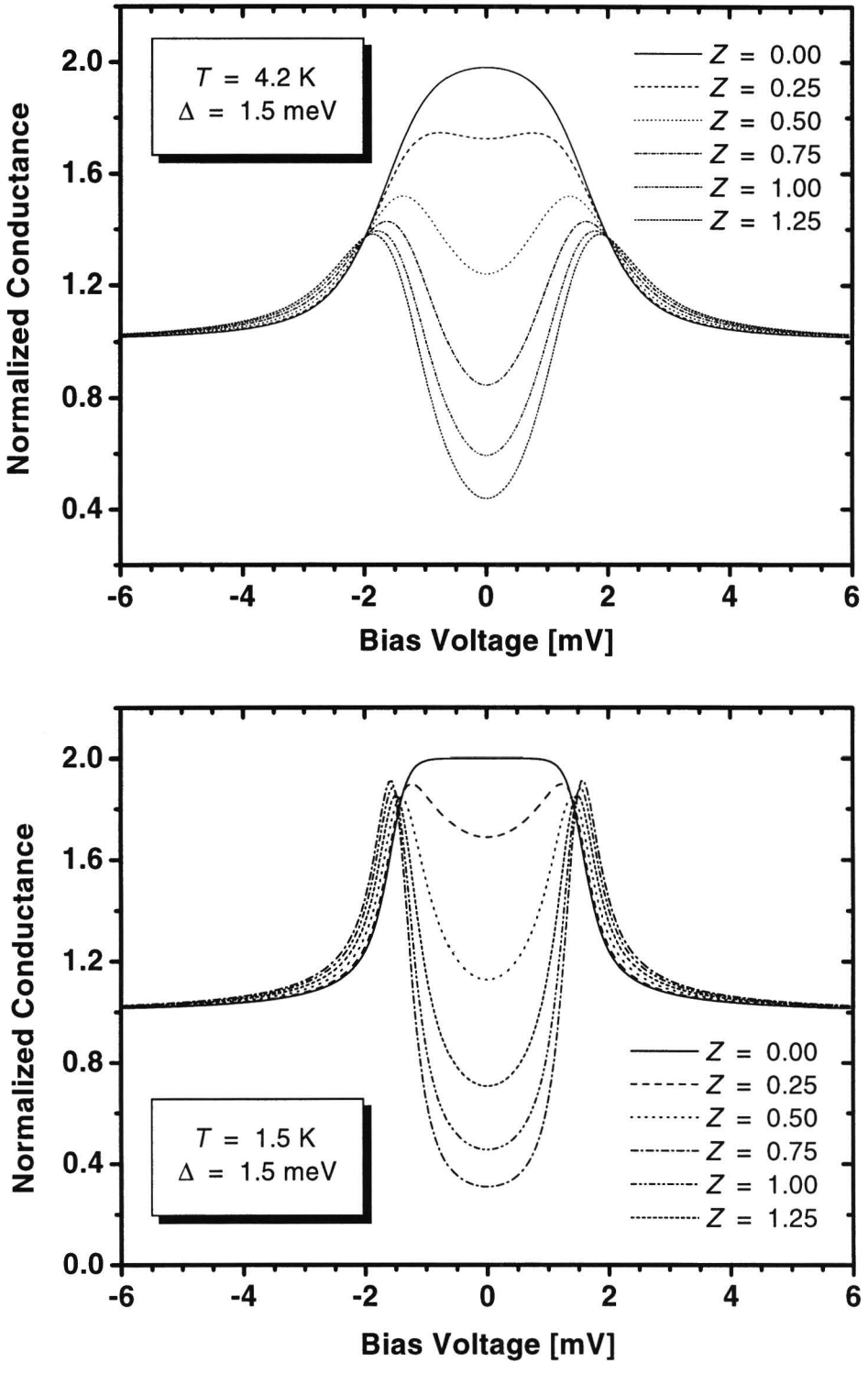

Figure 24: Normalized conductance according to the BTK model at temperatures 4.2 K (top) and 1.5 K (bottom) for various values of Z.

	Andreev reflection	Normal reflection
Nonpolarized N/S contact		
$E < \Delta$	$A(E)$	$B(E)$
100%-polarized N/S contact		
$E < \Delta$	$\tilde{A}(E)=0$	$\tilde{B}(E)=1$
$E > \Delta$	$\tilde{A}(E)=0$	$\tilde{B}(E) = \frac{1}{1-A(E)}B(E)$

Table 2: Probabilities $\tilde{A}(E)$ and $\tilde{B}(E)$ for a fully-polarized N/S contact, with $A(E)$ and $B(E)$ defined in Table 1 .

3.3 The modified BTK model including spin polarization

In Section 3.1, concerning the current through a polarized-normal-metal, the situation was approached by splitting up the current I in a current $I_\uparrow$ carried by the spin-up electrons and a current $I_\downarrow$ carried by the spin-down electrons. In calculating the current through a polarized-N/S contact, the modified BTK model uses the same type of approach: the total current through the contact I consists for a fraction $(1 - P)$ of a (nonpolarized) current carried by an equal number of spin-up and spin-down electrons, and for a fraction P of a (fully polarized) current carried by electrons with only one spin orientation:

$$I = (1 - P) \cdot I_{unpol} + P \cdot I_{pol}. \tag{53}$$

Determination of I_{unpol} and G_{unpol} versus V is discussed in the previous section. However, since Andreev reflection is impossible ($A(E) = 0$) for the electrons contributing to the polarized current, the probabilities $B(E)$, $C(E)$, and $D(E)$ have to be renormalized by the factor $1/(1 - A(E))$. This results in a new set of probabilities, given by (see also Table 2)

$$\tilde{A} = 0, \quad \tilde{B} = \frac{1}{1-A}B, \quad \tilde{C} = \frac{1}{1-A}C \quad \text{and} \quad \tilde{D} = \frac{1}{1-A}D. \tag{54}$$

The two contributions to the current (Equation 53) result in a similar way in two contribution to the normalized conductance. Given a the degree of spin polarization P, this reads

$$\left(\frac{G_{NS}}{G_{NN}}\right)_P = P\left(\frac{G_{NS}(\tilde{A},\tilde{B})}{G_{NN}}\right) + (1 - P)\left(\frac{G_{NS}(A,B)}{G_{NN}}\right). \tag{55}$$

Figure 25 displays the influence of P on the conductance curves at two temperatures with Z=0. As P increases, the zero-conductance $G_{NS}(V = 0)/G_{NN}$ decreases linearly by $2(1 - P)$ (as explained by Equation 38). For $P = 1$, only normal reflection is possible at $|eV| < \Delta$, resulting in G_{NS}=0. Similar curves at T=4.2 K are plotted in Figure 26, however with Z=0.25 and Z=0.5.

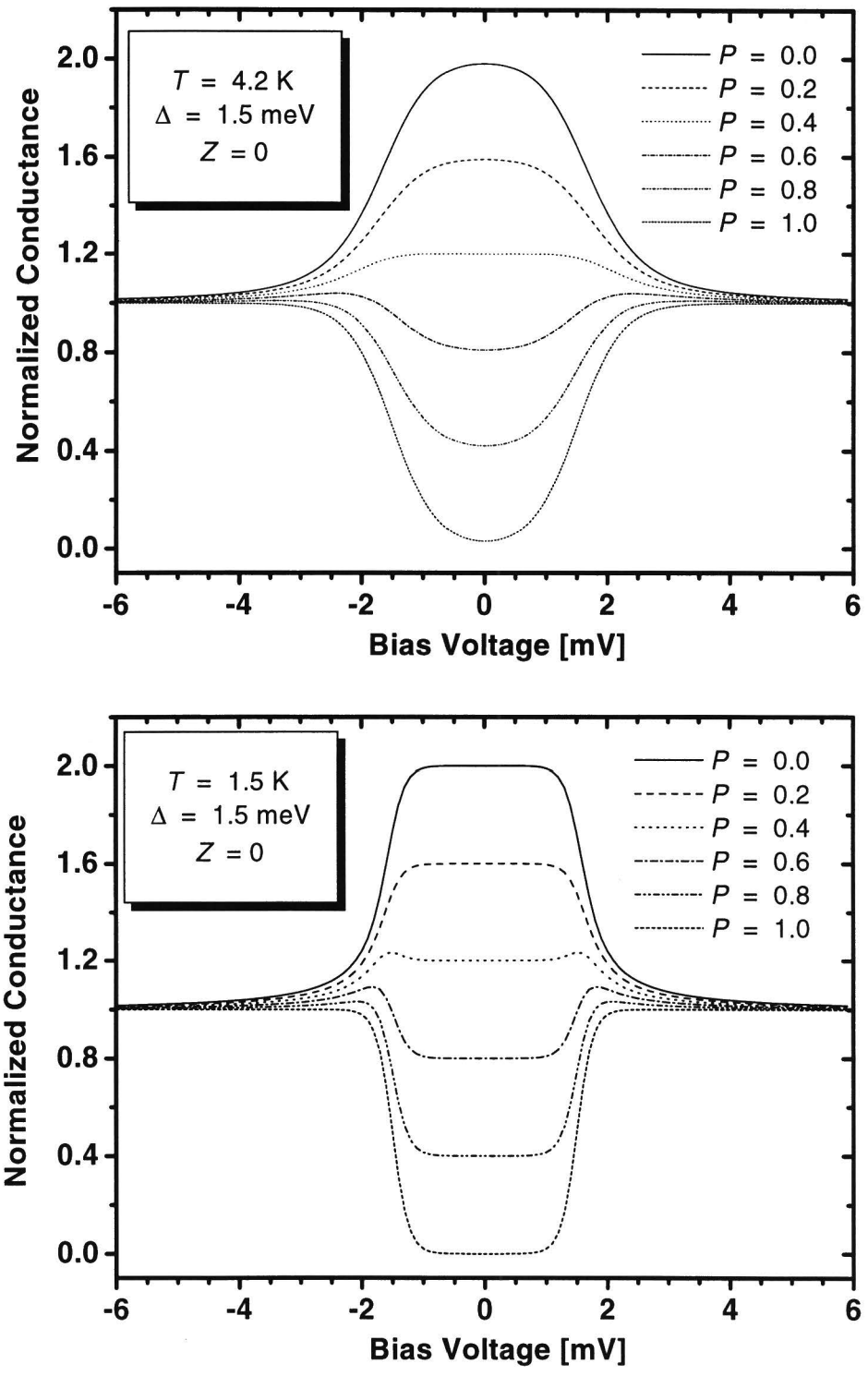

Figure 25: Normalized conductance according to the modified BTK model at temperatures 4.2 K (top) and 1.5 K (bottom) for Z=0 and increasing P.

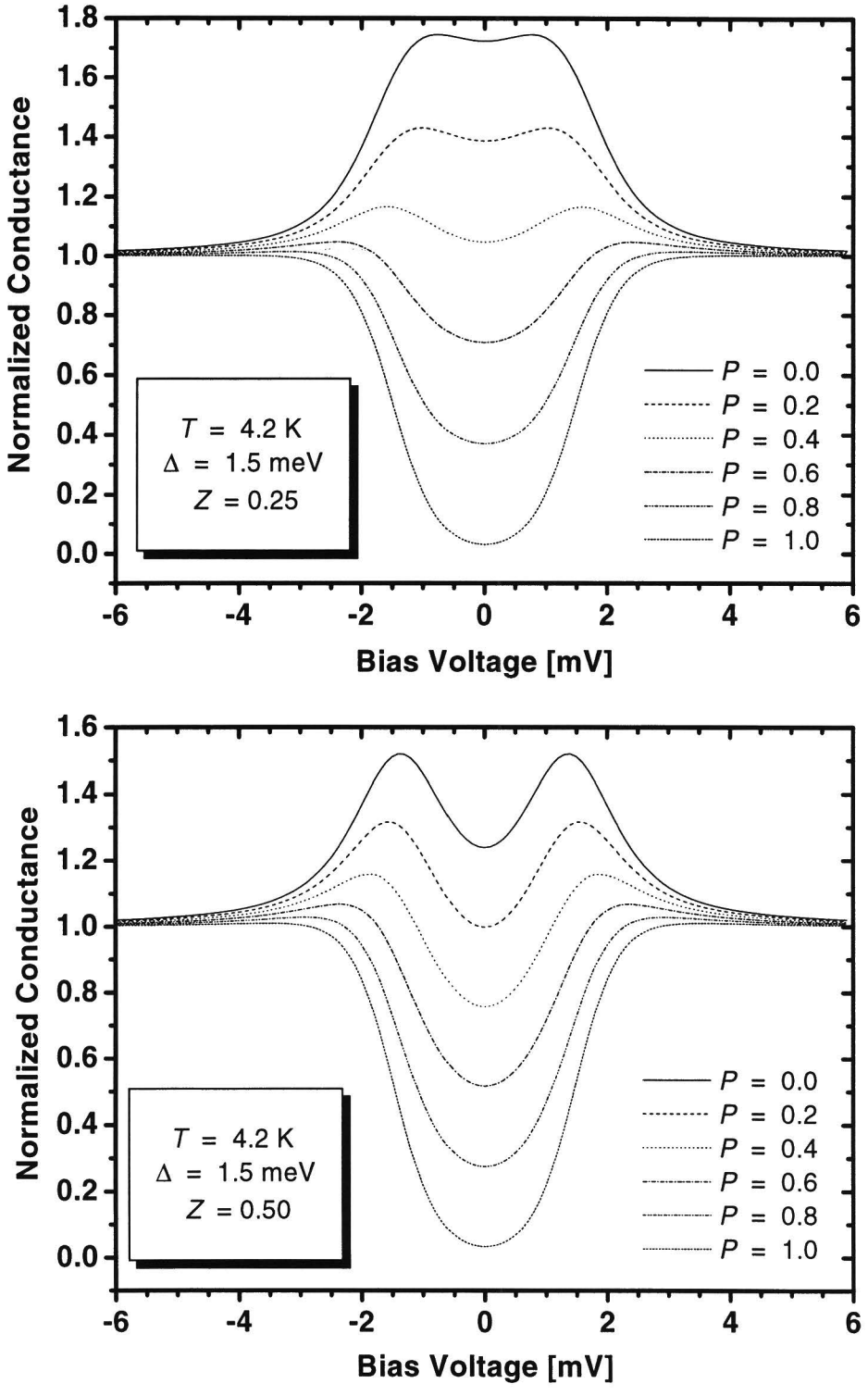

Figure 26: Normalized conductance according to the modified BTK model at 4.2 K and increasing P, for Z=0.25 (top) and Z=0.5 (bottom).

3.4 Fitting of measurements with the modified BTK model

The entire measured conductance curve (not only $(dI/dV)_{V=0}$) is fitted with the modified BTK model in order to extract values for the parameters Δ, Z, P, and T. However, due to limited resolution in the measurements and a theory based on various simplifying assumptions, data will never perfectly overlap a theoretical curve. Therefore, there is no unique set of extracted parameters. In other words, there is a finite uncertainty volume in the parameter space.

Analysis reveals that there are two regimes in which a small deviation between theory and measurements will result in an unacceptably large uncertainty volume in the parameter space. The first regime concerns measurements on contacts with $\Delta \approx kT$. The second regime concerns contacts with high-Z (Z approximately larger than 1). This can be seen as follows. In case of $\Delta \simeq kT$, the conductance maxima at $V = \pm\Delta$ are severely broadened. Consequently, the difference in dependence on P and Z is less clear. In case of $Z \gg 1$, the normalized conductance at zero bias is almost zero, regardless of P. Therefore, varying P will have negligible effect.

4 Experimental

Over the past years, various techniques have been used to create a point contact. Figure 27 summarizes the three most common contact schemes. The left image indicates how two materials can be deposited on a substrate (lithographic procedure) while forming a (point) contact [Jac00]. The second image shows two materials separated by an insulting layer containing a nano-hole [Upad98]. A straightforward method to create a point contact is illustrated in the third image. Basically, the contact is achieved by mechanically lowering a tip onto a sample. Mechanical movement can be controlled by a micrometer mechanism [Blo83, Sou98, Strij01] or by a piezo ceramic element. In the system described in this report the last option is chosen. This guarantees tip control on the Angstrøm scale, which is 1000 times smaller than the controlability obtained with the micrometer.

Details concerning the piezo control electronics in the system, the contacting procedure and the measurement electronics are well described in [Kant00]. The basics of the experimental setup and the contacting procedure will be shortly revisited in this chapter. Additional information on the piezo system, the cooling procedure and the preparation of the tip and sample will be given.

4.1 Overview of the setup

The main goal of the setup is to measure the current I through a contact as a function of an applied DC voltage V (four-probe measurement). However, more physical details can be extracted if not the I-V curve but the conductance curve dI/dV-V is analyzed. A standard LOCK-IN technique enables direct measurement of the conductance curve. This is done by superposing an AC voltage signal over the DC voltage. The AC signal can be regarded as a distortion dV ($dV = c\sin\omega t$). The current as a function of the applied voltage (DC plus AC component) can, via a Taylor expansion, be written as $I(V + dV)$=$I(V)$+$\frac{dI}{dV}dV$+.....

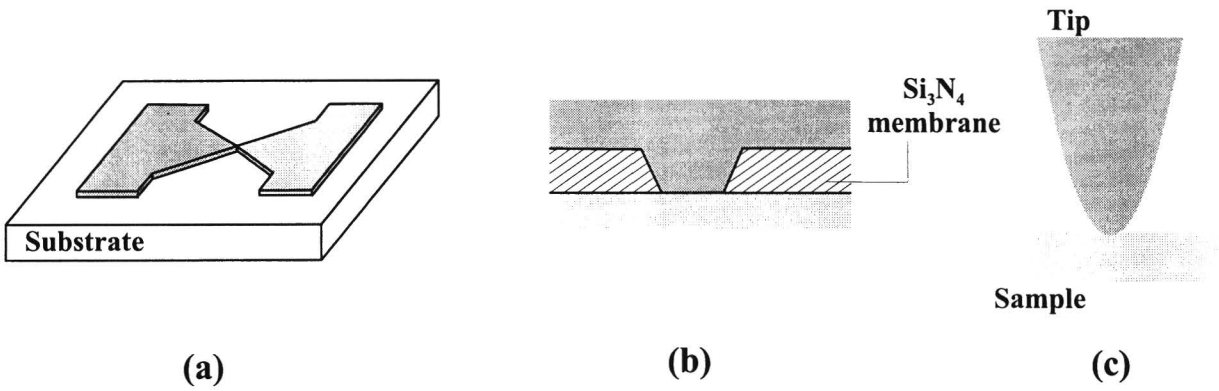

Figure 27: Point contacts realized by means of lithographic procedures (a), deposition onto both sides of an insulating membrane containing a nanohole (b) and by mechanically lowering a tip onto a sample (c).

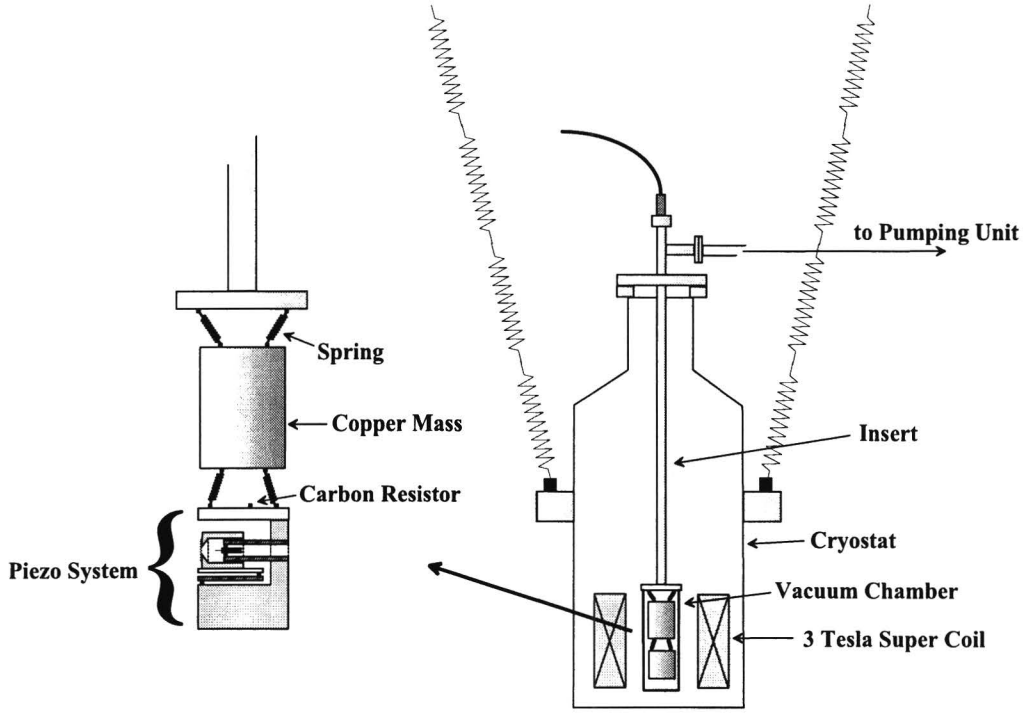

Figure 28: Schematic overview of the cryogenic part with the vibration insulation.

By neglecting higher-order terms one can retrieve

$$I(V + c\sin\omega t) \approx I(V) + \frac{dI}{dV} v \sin\omega t. \tag{56}$$

The LOCK-IN amplifier is sensitive for the AC signal at frequency ω only. Therefore, the LOCK-IN's output is proportional to dI/dV.

The setup is represented in Figure 28. The point contact is formed through the piezo system. This system, suspended by a mass-spring system to reduce vibrations, is located in a vacuum chamber which is part of the insert. The chamber is emerged in a liquid ^{4}He-bath and filled with the exchange gas for thermal contact between piezo system and the liquid He. A superconducting coil can generate a magnetic field up to 3 Tesla. However, during the present experiments no field is applied. The cryostat itself is also isolated from vibrations due to attached springs.

4.2 Contact formation by the piezo system

One unique characteristic of the setup is the precise controllability of the tip and sample, made possible by the piezo system showed with more detail in Figure 29. A piezo element has the characteristic that if a voltage is applied, the element will expand or shrink. The piezo elements in this setup give a change in length of several μm upon applying 500 V. This gives a controlled movement on the order of several Angstrøms. This, and the vibration insulation, allows gentle formation of the contacts.

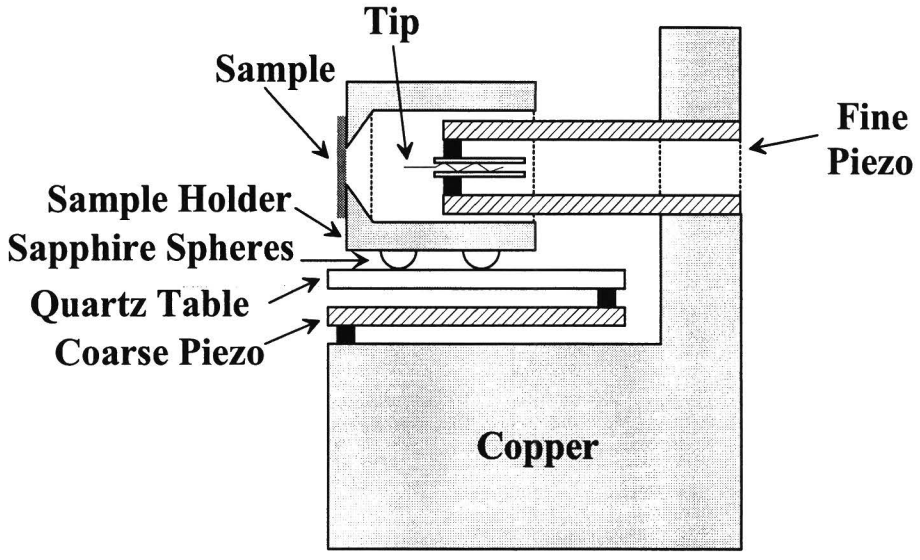

Figure 29: Schematic cross-section of the piezo system.

Stick-slip mechanism

The so-called stick-slip mechanism allows the sample holder to move over an unlimited range. Basically, one stick-slip action consists of the following two steps. 1) The coarse piezo is fully retracted, bringing the sample several μm closer to the tip. 2) The voltage over the coarse piezo is suddenly reduced to zero so that the piezo expands back to its original length. However, this time interval is too short for the sample holder to follow the withdrawing movement. A slip is initiated, resulting in a coarse piezo back in its original position and a sample holder several μm more close towards the tip.

Important for reliable sample holder movement is the 'low friction' sapphire/quartz contact between the sample holder and the table. In the first design of the piezo system, there was a direct contact between the copper sample holder and quartz table. Due to insufficiently low friction, the stick-slip mechanism was unreliable. The modification of adding sapphire spheres seems to be crucial.

Contacting procedure

At the beginning of the experiment, the sample and tip are separated several mm, and a 'coarse approach' procedure is initiated, which consists of the following three actions:

1. The fine piezo is expanded until a tunnel current of 80 pA is measured or until maximum expansion is realized.

2. If the fine piezo reaches its maximum expansion without sensing any tunnel current, the fine piezo is retracted to its original position.

3. The discussed stick-slip mechanism takes place. This subroutine consists of slow

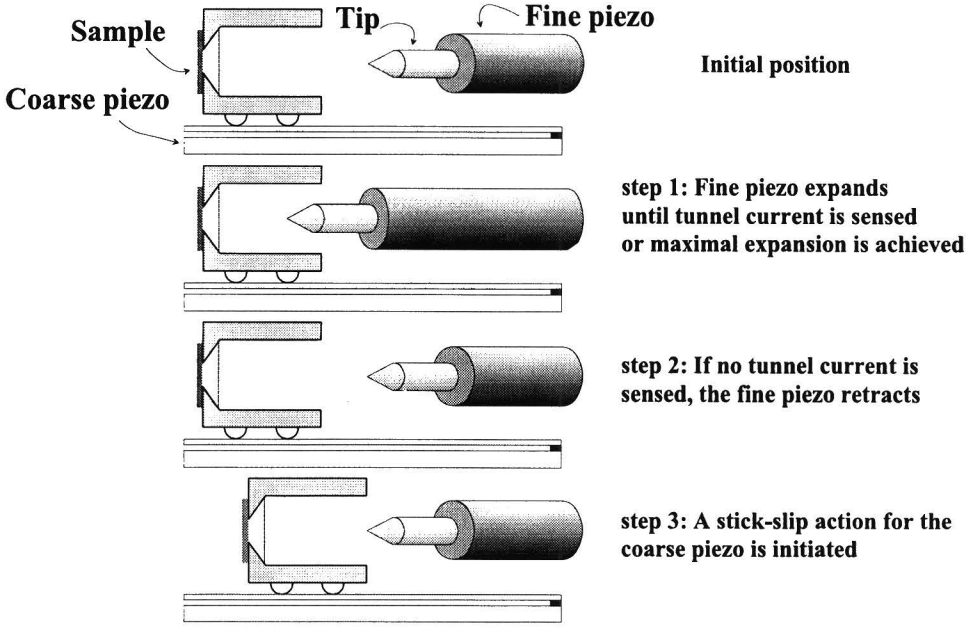

Figure 30: The three sketched steps indicate the actions taken during one 'coarse approach' procedure. The procedure is repeated until a tunnel current is sensed.

retraction and quick expansion of the coarse piezo and results in a net movement of the sample towards the tip.

The coarse approach continues until the tunnel current of 80 pA is measured and is automated and controlled by computer. There are several moments at which this procedure is initiated. At room temperature, in open air, this procedure will test the approach and bring the tip towards the sample. After succeeding in this, the sample is withdrawn from the tip (circa 500 reversed stick-slip actions). This is necessary due to accidental displacement of the sample during installation of the insert in the cryostat. This installation is followed by the second 'coarse approach' procedure (now in vacuum). After reaching the tunnel regime the sample is withdrawn only a few steps to anticipate vibrations and to prevent the premature formation of a point contact. The cooling process is now started. If no further testing would be performed, tens of thousands of stick-slip steps are needed, resulting in a time consuming coarse approach procedure for joining sample and tip at low temperature. This is a direct result of temperature dependent expansion and retraction of the piezo elements. To overcome this problem the coarse approach procedure is initiated for the third time at an intermediate temperature $T \simeq 100$ K.

In order to make the contact as gentle as possible, tunnel regime is used as a reference position. If a 80 pA tunnel current is measured at a 800 mV-bias voltage (R=10 GΩ), it is known that, for clean oxide-free surfaces, the tip is separated from the sample several Angstrøms. For such surfaces, expansion of the fine piezo will bring the tip and sample closer together, resulting in a smooth increase in current. However, discrete jumps are observed. This can be explained through the existence of an oxide layer between tip and

sample. If the resistance has dropped to 1-1000 Ω, it is believed that the tip has penetrated the oxide layer and that the metallic contact is formed.

By pushing the tip through the oxide, the tip will be plastically deformed. It can become blunt and therefore the probability to obtain contacts which have a radius smaller or comparable to the mean free path is reduced by the presence of the oxide. This probably explains why circa 75% of the measurements produce conductance curves that do not resemble curves predicted by the modified BTK-model, which is valid for ballistic contacts only.

4.3 System cooling

After the insert is lowered into the cryostat, the vacuum chamber is pumped down to remove all air, followed by injecting exchange gas. This gas realized the thermal contact between the piezo system and the helium bath. Liquid ^{4}He can be transported from a storage dewar into the cryostat. The temperature in the vacuum chamber will reach 4.2 K (the boiling temperature for liquid ^{4}He).

There are several reasons why measuring at 1.4 K is preferred. 1) The liquid ^{4}He at 4.2 K, surrounding the vacuum chamber, has a relatively low thermal conductivity, resulting in vibrations due to boiling. At 1.4 K, the liquid ^{4}He is superfluid (λ-temperature $T_\lambda = 2.18$ K) and boiling occurs without bubbles due to relatively high thermal conductivity and vibrations are reduced. 2) At a lower temperature, the thermal smearing will become less. This is accompanied by 'sharper' measured conductance curves so that fitting will yield more accurate fitting parameters. Below it is classified how this lower temperature can be realized.

Consider the liquid/vapor ^{4}He-bath. Removal of ^{4}He-vapor by means of pumping will

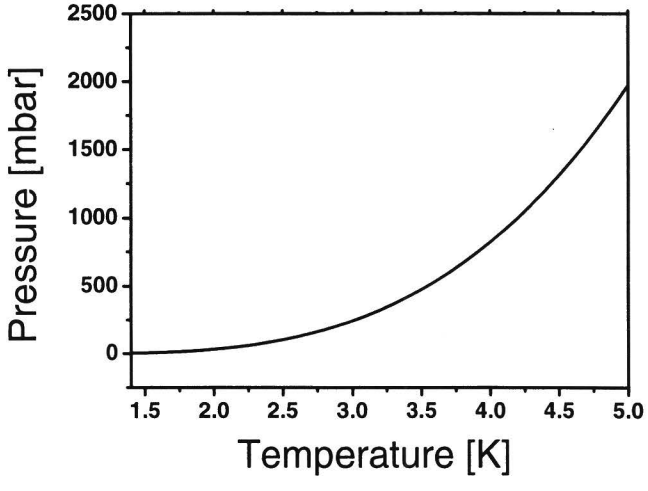

Figure 31: Pressure of the vapor in a vapor/liquid system for ^{4}He, taken from [Pob96] (note the T=4.2 K at p=1 bar).

	Pb	Nb
type	I	II
Δ [meV]	1.37	1.53
T_c [K]	7.19	9.50
$H_{c(1)}$ [kA/m]	63.9	128
ξ [nm]	83	38

Table 3: Bulk properties of the superconductors Pb and Nb, taken from [Kit96].

result in a reduction of the vapor pressure with a corresponding reduction of overall temperature. After a while, an equilibrium vapor pressure has established because the same amount of vapor that is pumped away is supplied through evaporation. Due to the presence of the contact gas in the closed chamber, the temperature inside the chamber will drop as well and the original gaseous contact gas will condensate: a new closed liquid/vapor system is formed. Measurements done on a comparable closed ^{4}He liquid/vapor system result in the curve in Figure 31. The setup uses a rotary pump with a pumping capacity of 200 m^3/hour that can reduce the vapor pressure to circa 4 mbar which corresponds to a temperature of 1.41 K.

4.4 Tip and sample preparation

In all experiments described in this report, lead (Pb) or niobium (Nb) tips are used. The bulk values for the superconducting bandgap Δ, coherence length ξ, critical temperature T_c, and the critical field $H_{c(1)}$ are displayed in Table 3.

In order to form a point contact, a tip has to be prepared with a sufficiently small radius of curvature (see Section 2.2). Three different methods for realizing this sharpness are mechanically polishing, cut-and-pull, and a 'tilted-sample' tip. These methods are described below.

A mechanically polished tip is prepared by clamping a 1-mm wire into a drill. The rotating wire is then softly pressed to a fine structured piece of sandpaper ($\approx$1 grain/μm^2). Subsequently, the tip is examined under a microscope to check that the radius of curvature

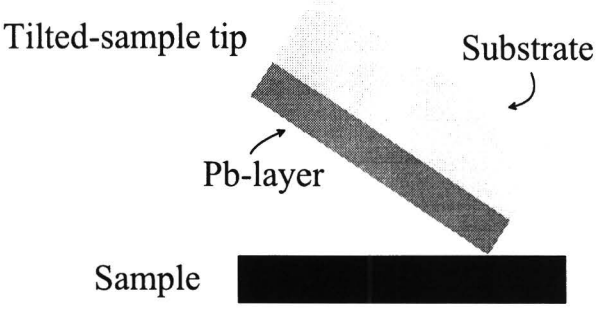

Figure 32: Schematic representation of a 'tilted-sample' tip.

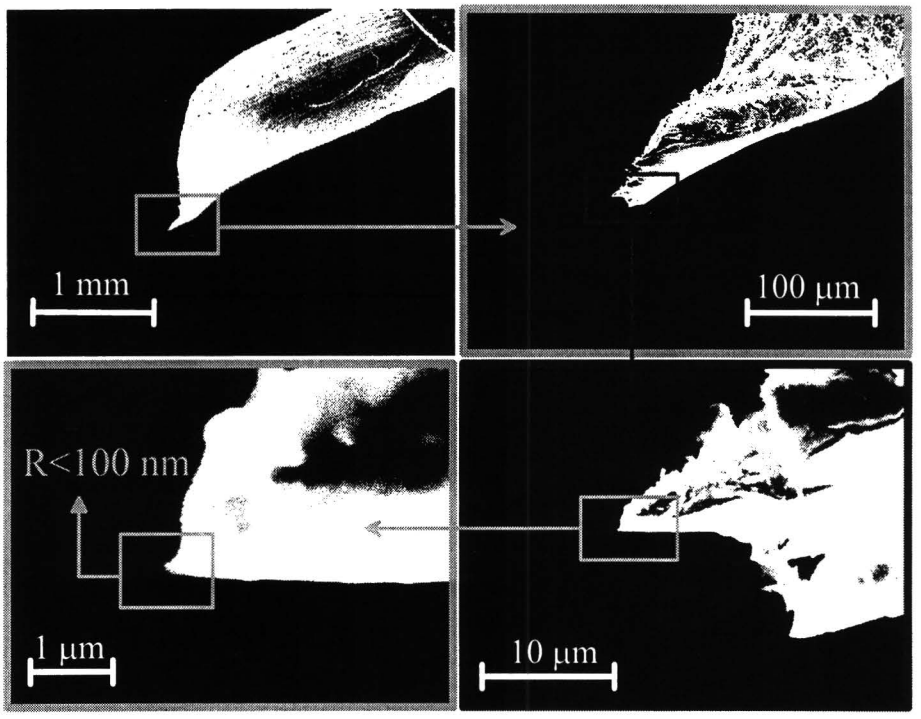

Figure 33: Four SEM-images taken on the same tip (prepared by cut-and-pull), with increasing magnification.

is less than 1 μm. Some measurements using tips prepared in this way have been successful, meaning that the obtained dI/dV-V curves are consistent with the modified BTK model (Chapter 3) which is only valid for contacts in the ballistic regime. The tips obtained with this method are well defined (sharp polished end) but, since the tip is polished against structured surfaces, it is not perfectly clean.

A similar tip configuration (however faster and easier to prepare) is obtained through the so-called cut-and-pull method. A 1-mm wire is simple cut by a pair of scissors. A pull is enforced just before the wire is split in order to create a clean surface. Although the tip is not well defined, small 'mini-tips' on the surface are always present and provide the demanded radius of curvature. SEM-images confirm the presence of 'mini tips' with a curvature $a \leq$100 nm (Figure 33). Also attempts with such tips have been successful.

A third attempt for sharp-tip configurations consists of evaporating a thin (100-1000 Å) Pb-layer on top of a substrate. By tilting the film, (Figure 32), the radius of curvature must be lower than the Pb-layer thickness, at least in two dimensions. Such tips are both well defined and clean. However, measurements do not resemble the theoretical predicted curves in the ballistic regime (BTK model). Microscope images taken before and after measurements reveal that the Pb-layer has crumbled off, probable due to bad adhesion of Pb to the substrate. This can result in a contact between the substrate part of the 'tilted-sample' tip and the sample. To date, tips of these kind have not been successful.

Samples prepared by various techniques have been used. One technique concerns the use of a bulk metal, that has been chemically treated in an attempt to obtain a smooth

surface. Other samples are prepared by sputtering the metal onto a substrate, and (in some cases) an additional capping layer of Au was deposited since. Au is believed not to oxidize. Since no correlation between sample preparation and the chance of a successful measurement is found, no further attention to sample preparation is given.

5 Results

This section will only focus on those contacts that resemble curves in agreement with the modified BTK model (valid in the ballistic regime). The first two sections give a general overview of the experiments. Section 5.3 discusses the relation of the spin polarization on the interfacial scattering. Also the superconducting bandgap seems to depend on the contact properties, which will be treated in Section 5.4. The (partial) destruction of superconductivity is shown for a series of measurements in the last section.

5.1 General measurement phenomena

Section 4.2 argued that the presence of an oxide layer complicates the formation of ballistic or quasi-ballistic contacts. This section focuses only on those measurements that do resemble the modified BTK-model (Chapter 3), which is valid only in the ballistic regime.

All conductance curves are normalized with respect to the constant conductance measured at $|eV| \gg \Delta$. The fits are carried out while allowing variation of all parameters $\{T, \Delta, Z, P\}$. Generally, the temperature T obtained from the fit is higher than the experimental temperature (4.2 K or 1.4 K), as is shown in two typical measurement in Figure 34. In [Kant00], the following explanation for this effect is proposed. The bandgap is modeled to increase abruptly from 0 in N to Δ in S. However, in reality the interface is smeared and its effect can lead to an apparent T higher than the experimental T. Another possible explanation is the effect of local heating due to the current through the contact. In the coming sections, no further notion is given to the deviation between fitted and experimental temperature.

Figure 34 also indicates the presence of excess conductance with respect to the BTK model, starting at $|eV|/\Delta \simeq 1-2$ and ending at $|eV|/\Delta \simeq 4-5$. Several possible

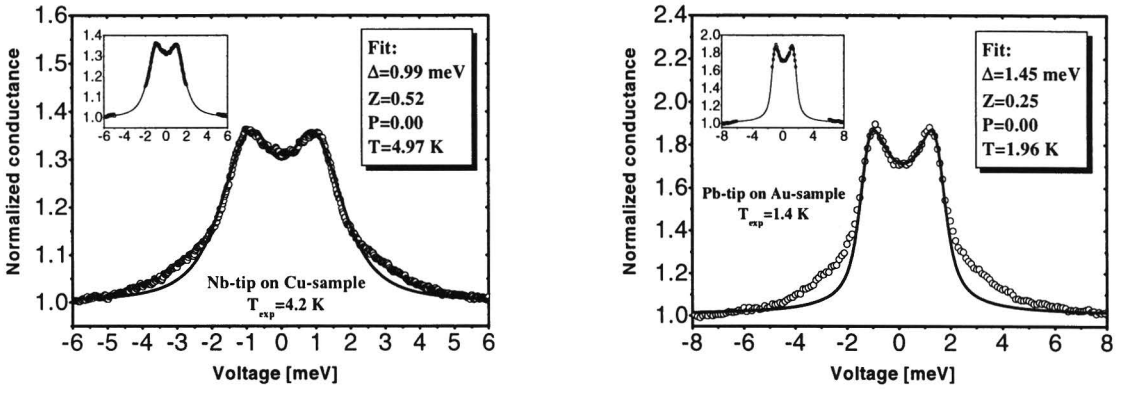

Figure 34: Two representative curves for a Cu/Nb and Au/Pb contact, measured at 4.2 K and 1.4 K respectively. The solid line through the data points is a fit with the modified BTK model. The fits do not use the complete measured curve, as shown in the insets.

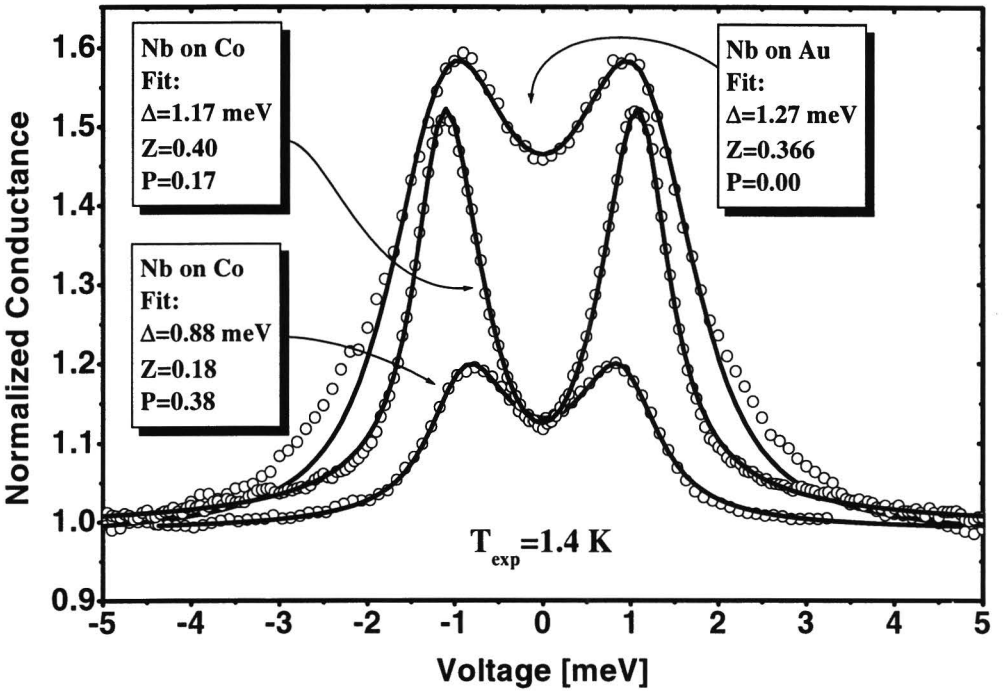

Figure 35: Measurements on two Co/Nb contacts and (for reference) on a Au/Nb contact. The reduction in normalized conductance for Co/Nb is a consequence of its nonzero spin polarization. The solid curves represent the fits with the modified BTK model

explanations for this effect can be given. First of all, the formed contact can have a radius a comparable to the mean free path l, while the modified BTK model assumes $a \ll l$. Furthermore, the BTK-model includes only elastic scattering and no inelastic processes.

5.2 An overview of measured and fitted conductance curves

Measurements on nonpolarized- and polarized-N/S contacts

Measurements on contacts Co/Nb and Co/Pb contacts (ferromagnetic Co is known to have a nonzero spin polarization) show curves like the ones plotted in Figure 35. The fits with the modified BTK model indicate a difference in P for the two Co contacts. This phenomenon will be discussed in Section 5.3. To highlight the influence of the polarization on the normalized conductance, a measurement of Nb on Au is shown also. As expected, the fit for the Au/Nb contact yields $P = 0.00$. Note that the value $P = 0.000..$ is frequently extracted from fits, since it represents the lower boundary of the P-domain ($0 \leq P \leq 1$).

Measurements in the high-Z regime

Several measurement have shown conductance curves as in Figure 36, with a relatively high resistance (70 kΩ) and a relatively high extracted value for Z ($Z = 2$). It is believed

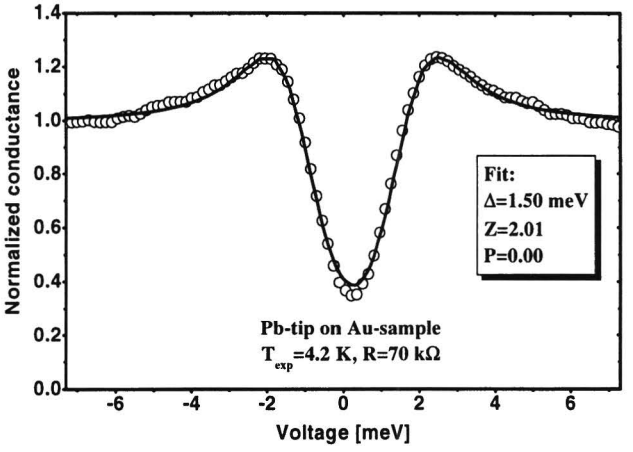

Figure 36: Conductance curve for a Au/Pb contact (note the high resistance!) with probably a thin oxide layer at the interface (N/I/S contact). Such a contact can be also represented as an N/S contact with high Z, as is confirmed by the BTK fit (solid line).

that for such contacts, a thin oxide layer still exists between tip and sample. Since the conductance at V=0 has a nonzero value, one can not compare this contact regime with a high-quality tunnel junction, where the conductance is zero at subgap voltages.

A measurement series on one stable contact

Several series of conductance curves on the same stable contact have been measured. One series of experiments that this was possible, concerned measurements on Co/Nb contacts. By varying the tip pressure, circa 15 curves were obtained. Four of those curves are displayed in Figure 37. Their fits show a change in values for R, Δ, Z and P, which will be part of the discussion in the coming sections.

5.3 Dependency of interfacial scattering on the DSP

The four curves plotted in Figure 37 suggest that there is a correlation between P, R, and Z. According to $R = R_0(1 + Z^2)$ (Equation 12) for $0.4 < Z < 0.5$, a change in R of several percent is expected. However, a change of 100-400% is observed, see Figure 38. Apparently, for the series of measurements performed on this contact, the influence of Z on R is negligible and the differences in R are probably a result of the changing contact radius a. The question now is, does P depend on Z, on R (and thus a), or on a combination of both?

The values for P extracted from the previously mentioned Co/Nb series, as well as the values obtained from all other measurements on Co, are plotted as a function of R and Z in Figure 39. It seems that there is no correlation between P and the resistance (left plot). However, as a function of increasing Z, the spin polarization tends to decrease

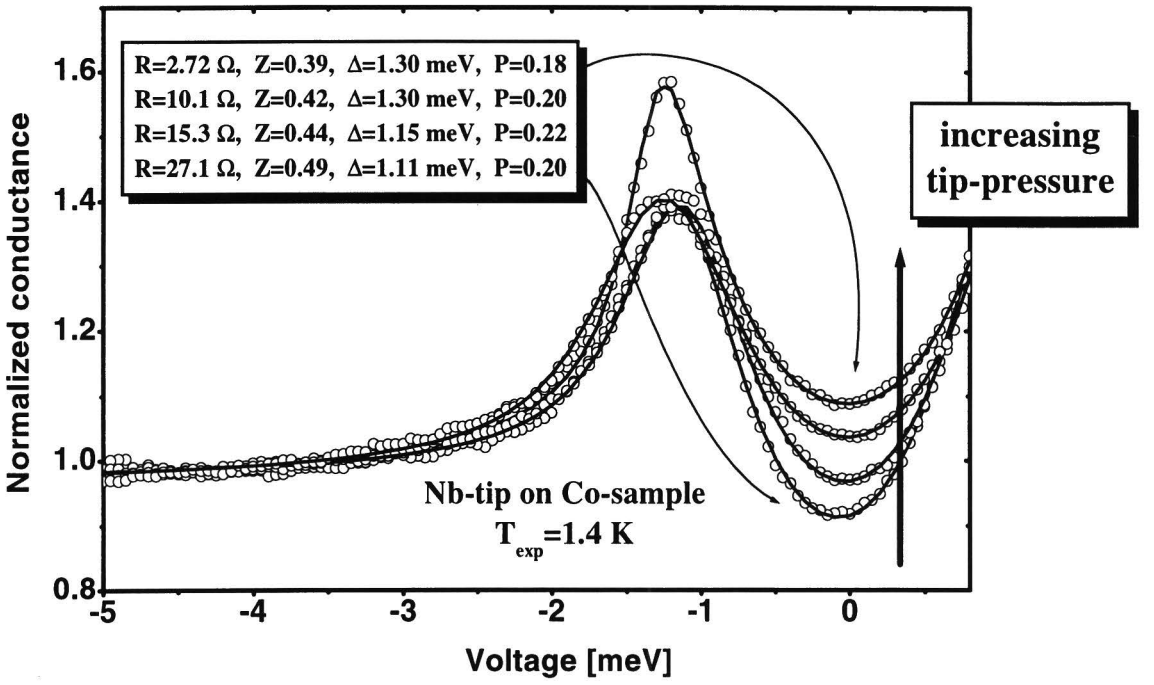

Figure 37: Four conductance curves, part of a series of measurements performed on one stable contact (Co/Nb). The solid lines represent the fits with the modified BTK model.

to zero, as is illuminated by a guide to the eye. Strijkers [Strij01] observed the same phenomenon (see Figure 40. He suggested that the interfacial scattering is accompanied by an increase in spin-flip scattering. Although so far no theoretical base has been given, one can expect that, since spin-flip scattering tends to balance the number of spin-up and spin-down electrons, a lower P should be measured. To Figure 40, the 'guide to the eye'

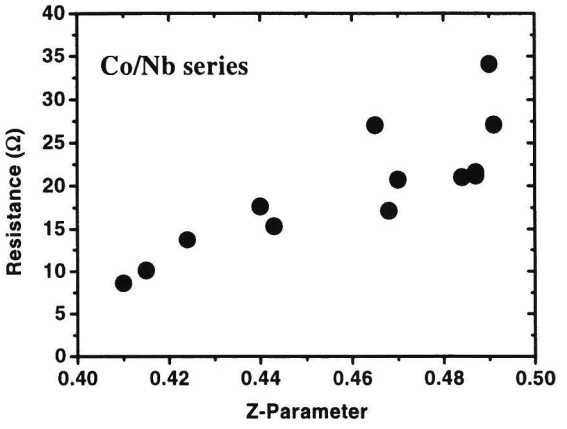

Figure 38: The series of curves on the stable Co/Nb contact yield the plotted R-Z correlation.

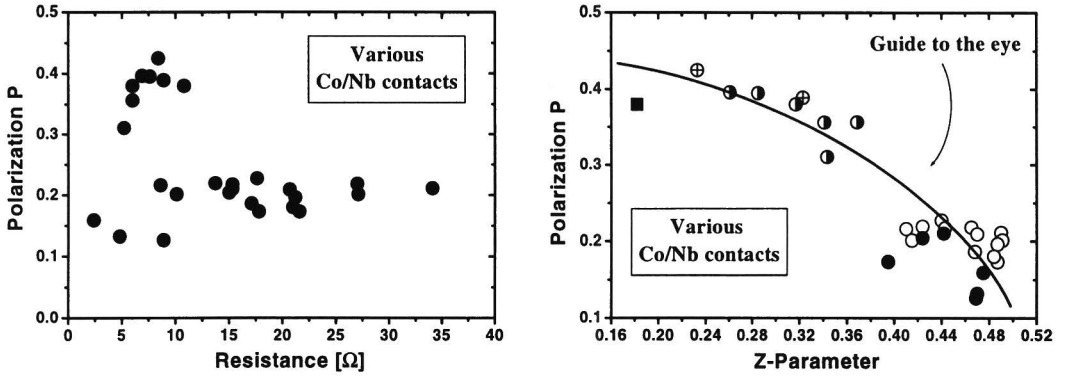

Figure 39: If one plots P versus R (left), no correlation can be found. However, P versus Z (right) shows a decrease of spin polarization at higher barrier strengths Z.

from Figure 39 is appended.

In order to give the intrinsic spin polarization of Co, one should use the value closest to $Z = 0$. Since it is not completely sure that the contacts are in the ballistic regime, one can not say that this spin polarization is purely the P_{Nv}, as defined in Equation 5.

5.4 Observation of decay in the superconducting bandgap

The four representative curves in Figure 37, part of a measurement series on Co/Nb, indicate a decay in the bandgap as a function of resistance R. The intuitive model presented in Section 2.5 attributes such behaviour to the fact that the contact radius a is smaller than the coherence length ξ. In Figure 41, the extracted values for Δ are plotted as a function of R.

The solid line in Figure 41 is a fit with Equation 36. The parameters p_1 and p_2 are defined in Equation 37 and their extracted values are 0.86±0.03 meV and 0.8±0.1 $\Omega^{-1/2}$

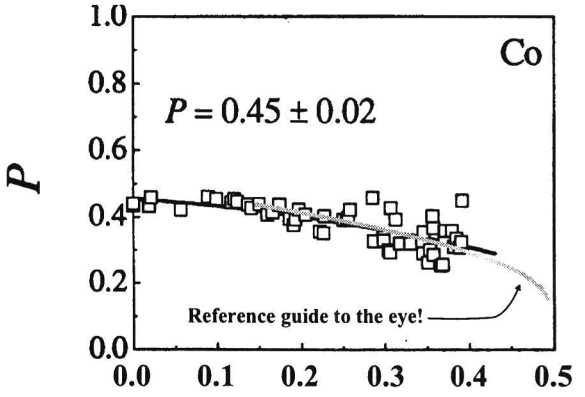

Figure 40: Relation between P and Z as observed by Strijkers *et al* [Strij01], indicating a decrease in P with interfacial scattering Z. The 'guide to the eye', drawn in Figure 39, is appended as reference.

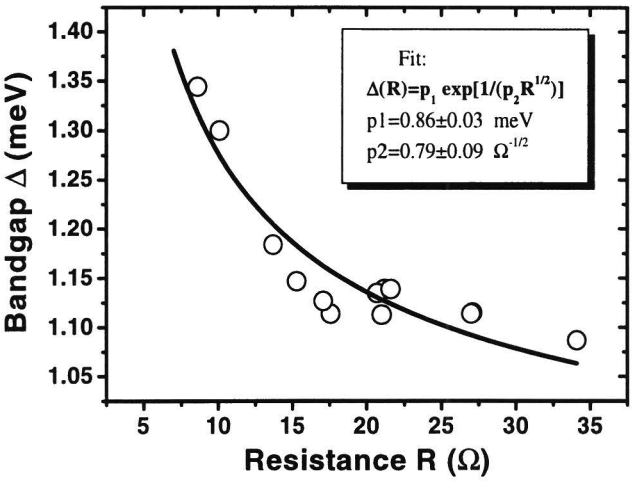

Figure 41: Illustration of the decay of the bandgap Δ as a function of resistance, for a Nb tip on Co. The solid line is a fit with the geometrical intuitive model.

respectively.

It is impossible to solve Δ_0, ξ and θ from the two extracted values for p_1 and p_2. However, one can give an estimation for θ. For $30° < \theta < 60°$ one obtains $1.0 < \Delta_0 < 2.3$ meV and, by using the ballistic approach $a\sqrt{R}$=20 nm$\sqrt{\Omega}$, $9 < \xi < 27$ nm. The extracted values are in reasonable agreement with the bulk values Δ=1.5 meV and ξ=38 nm, certainly in view of the simplicity of the model.

5.5 Destruction of superconductivity due to generated fields higher than the critical field

It was introduced in Section 2.4 that the current, at voltage V_c, through a superconducting tip can generate a field $H > H_c$. One series of measurements (Pb on Au) shows the existence of the voltage peaks and is plotted in Figure 42. The curves are measured with the same tip and the tip-pressure is varied to realize contacts with various resistances. In other words, the series is not the result of a continuously increasing tip-pressure.

The figure clearly shows a decrease in V_c for decreasing resistances. The 350 Ω-contact has a resistance that is too high for observation of V_c within the 5 meV-voltage range. If one disregards the critical peaks, the conductance curves can be reasonably fitted with the modified BTK model (solid lines). This suggests that the contacts are ballistic ($a \ll l$) or quasi-ballistic ($a \approx l$).

The model proposed in Section 2.4 predicts that for the position of the voltage peaks obey the correlation $V_c = k\sqrt{R} + V_0$. The measured values for V_c and $\sqrt{R}$ are plotted in Figure 43. The linear fit yields $k = 0.21 \pm 0.04$ meV/$\Omega^{1/2}$ and $V_0 = 0.9 \pm 0.2$ meV.

From the slope k, the critical field can be calculated using Equation 31 and

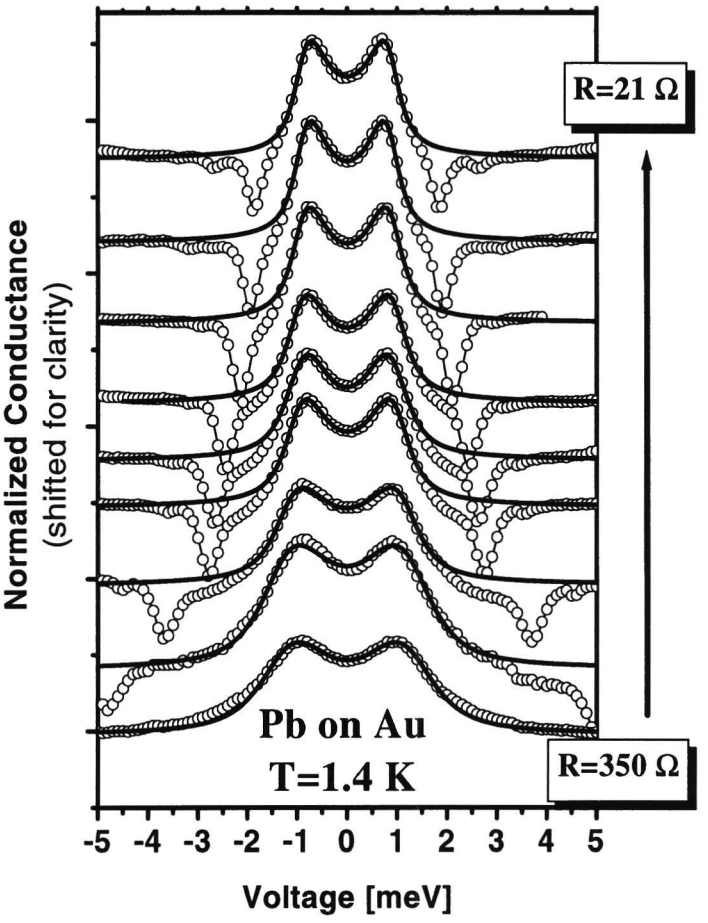

Figure 42: A series of conductance curves measured on one Au/Pb contact, showing the destruction of superconductivity at $\pm V_c$. As the resistance decreases, the position of V_c shifts towards $V = 0$. The solid lines represent the fits with the modified BTK theory.

$a\sqrt{R} \simeq 20$ nm$\sqrt{\Omega}$, resulting in H_c=1.7 kA/m. The bulk value for Pb is given by 64 kA/m, which is factor of 30 higher than the observed H_c. A possible explanation for this is influence of the tip geometry on H_c. Westbrook and Javan measured with a normal tip (W) on a superconductor (Ta) a reduction of 2 for the H_c. One must realize that the influence of the geometry on H_c for an S-tip on an N-sample can be completely different than for an N-tip on an S-sample.

As a check of consistency, one can extract the mean free path from the measured value V_0, providing that an estimation of $I_{exc}(\Delta)R$ can be given. Figure 44-(a) and (b) shows the extracted values for Δ and Z as a function of R. One can roughly conclude that Δ and Z are constant, resulting in the conclusion that also $I_{exc}(\Delta)R$ can be regarded constant in all curves. Its value is extracted from $I - V$ data and gives $I_{exc}(\Delta)R \approx 0.1$ meV. This value and the extracted H_c can give an rough estimation for l, namely l=2-3 nm. This value is consistent with the assumption of a quasi-ballistic contact, since the values of R_N

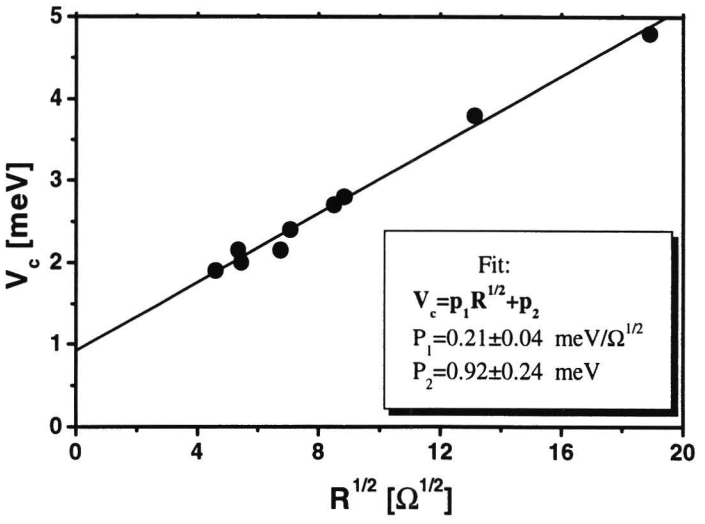

Figure 43: The plot displays the values of V_c versus $\sqrt{R}$, to which a linear fit is applied.

correspond to contact radii on the order of several nm.

Not all contacts show similar critical peaks. One explanation for this is that for most contacts, the H_c is too high for the peaks to lie within the measurable range. Probably, the shape of the Pb-tip used for these specific measurements has a rare and 'special' geometry. This can also explain why for this contact a decay in bandgap versus R is not observed, since probably the geometry differs too much form the cone-shaped tip used in the intuitive model presented in Section 2.5.

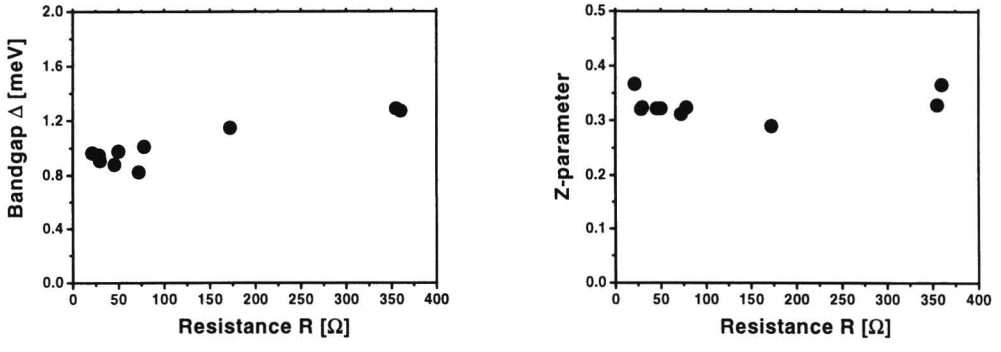

Figure 44: The extracted parameters Δ (left) and Z (right) as a function of the Au/Pb contact resistance R. In a rough approach, Δ and Z can be considered constant.

6 Conclusions and Suggestions

The most important conclusion that can be drawn from all performed measurements, is that the realization of (quasi-)ballistic N/S contacts is not a controlled process and is accompanied by a small chance of success. Since tip and sample are prepared in open air, the presence of an oxide layer is unavoidable. The superconducting tip has to penetrate this layer be means of severe increase of tip-pressure, which is accompanied by deformation of its end and/or the creation of a blunt tip. The majority of the measured conductance curves does not resemble the modified Blonder-Tinkham-Klapwijk (BTK) model (valid in the ballistic regime), but shows features probably related to transport phenomena in the so-called mesoscopic regime ($a > l$, with a the contact radius and l the electron mean free path). Since both tip and sample are believed to be deformed in the contact formation, studies on thin (10-100 $\AA$) metallic films seem not possible. Also, the idea of capping the metallic layer by Au (Au is believed to contain no oxide layer), does not improve the succes in formation of a (quasi-)ballistic contact. This suggests that tip preparation is more important than important than sample preparation.

However, still a number of N/S point contacts have successfully been realized, both on nonpolarized as well as on polarized normal metals. The obtained results are in the ballistic ($a \ll l$) or quasi-ballistic ($a \simeq l$) regime.

The measurements show that the extracted degree of spin polarization (P) on Co contacts decreases as a function of the elastic scattering parameter Z, from $P \simeq 0.40$ at $Z = 0.2$ to $P \simeq 0.15$ at $Z = 0.5$. This can be understood if one relates an increase in Z to an increase in spin-flip scattering, which levels out a difference in the number of spin-up and spin-down electrons. More insight in this behaviour can be acquired if one could extract values for P at $Z < 0.2$ and $Z > 0.5$. Another challenge is the understanding of the physics behind spin-flip scattering and its influence on P.

Another result is obtained on various measurements on a single stable Co/Nb contact, while increasing the tip-pressure (and therefore increasing the contact size). Am exponential decay in the extracted superconducting bandgap Δ is observed if one plots Δ versus $1/\sqrt{R}$, with R the contact resistance which is directly related to the contact radius. This exponential decay reasonably matches an geometrical intuitive model, based on the fact that the Cooper pairs (with characteristic length ξ) do not fit inside the sharp end of the tip. In fact, a fit with this model extract parameters for Δ_0 and ξ, which have comparable magnitude to bulk values. This interesting result has not been reproduced yet. Furthermore, future research can focus on a more profound theoretical basis.

If the tip has a sufficiently low critical field H_c, the destruction of superconductivity is observed at voltages $\pm V_c$ within the measurable voltage range. Conform the Westbrook-Javan model, measurements on Au/Pb contacts show there is a linear dependency between V_c and $\sqrt{R}$. The slope yields information about H_c, while the offset at $R = 0$ can give an estimation for l. Westbrook and Javan founded their model to measurements of an N-tip on an S-sample! They extracted a H_c that is twice as small as the bulk value. However, an S-tip on an N-sample is probably accompanied by a larger reduction of the critical field. This, combined with a possible 'special' tip geometry, can explain why the extracted H_c,

for the measurements described in this report, is 30 times smaller than the bulk value. The reason why the tip geometry is believed to play a role, is because other N/S contacts (even low-Ohmic contacts) do not show the destruction of superconductivity. Apparently, the H_c (and therefore V_c) is too high to be realized within the measurable regime. Studying the critical field of a superconductor in proximity with a normal metal with this method deserves more attention, specially because in the last couple of years proximity effects have gained significant interest.

In order to increase the chance of succes for formation of (quasi-)ballistic contacts, and to minimize tip and sample deformation in the process, still the correct method for tip preparation has to be found and accordingly a better yield of succes can be expected in the future. One idea is giving an additional chemical treatment to the tip after it has mechanically been polished, resulting both a well defined and clean tip.

Needless to say, the ideal experimental setup for this type of measurements would be *in-situ* Low temperature STM, capable of performing four-probe measurements, which is necessary for contacts in the range 1-1000 Ω.

References

[And64] A.F. Andreev, Zh. Eksp. Teor. Fiz. **46**, 1823 (1964) [Sov. Phys. JETP **19**, 1228 (1964)]

[Bai88] M.N. Baibich *et al, Giant Magnetoresistance of (001)Fe/(001)Cr Magnetic Superlattices.* Phys. Rev. Lett **61**, 2472 (1988)

[Bar61] J. Bardeen, *Tunneling from a many-particle point of view.* Phys. Rev. Lett. **6**, 57 (1961)

[Bass82] J. Bass, *Landolt Börnstein New Series, edited by K.H. Hellwege and J.L. Olsen.* (Springer, Berlin, 1982, Vol. 3/15a)

[BCS57] J. Bardeen, L.N. Cooper and J.R. Schrieffer, Phys. Rev. **106**, 162 (1957); Phys. Rev. **108**, 1175 (1957)

[Been97] C.W.J. Beenakker, *Random-matrix theory of quantum transport.* Rev. Mod. Phys. **69**, 731 (1997)

[Blo83] G.E. Blonder, and M. Tinkham, *Metallic to Tunneling Transition in Cu-Nb Point Contacts.* Phys. Rev. B **27**, 112 (1983)

[BTK82] G.E. Blonder, M. Tinkham and T.M. Klapwijk, *Transition from Metallic to Tunneling Regimes in Superconducting Microconstrictions: Excess Current, Charge Imbalance and Supercurrent Conversion.* Phys. Rev. B **25**, 4515 (1982)

[Coo56] L.N. Cooper, Phys. Rev. **104**, 1189 (1956)

[Frö50] J. Fröhlich, Phys. Rev. Lett **6**, 57 (1961)

[Gri95] D.J. Griffiths, *Introduction to Quantum Mechanics.* (Prentice Hall, 1995)

[Jac00] M. Jacob *et al, Direct Determination of the Andreev Reflection Probability by means of Point Contact Spectroscopy.* Appl. Phys. Lett. **76**, 1152 (2000)

[Jan89] A.G.M. Jansen *et al, Point contact spectroscopy.* Phys. Condens. Matter. **1**, 3157 (1989)

[Ji01] Y. Ji *et al, Determination of the Spin Polarization of Half-Metallic CrO_2 by Point Contact Andreev Reflection.* Phys. Rev. Lett. **86**, 5585 (2001)

[Jong95] M.J.M. de Jong and C.W.J. Beenakker, *Andreev Reflection in Ferromagnet-Superconductor Junctions.* Phys. Rev. Lett. **74**, 1657 (1995)

[Jul75] M. Julliere, *Tunneling between Ferromagnetic Films.* Phys. Lett. **54A**, 225 (1975)

[Kant00] C.H. Kant, *Spin Polarization in Andreev Point Contacts.* (master thesis, Eindhoven University of Technology, Eindhoven, 2000).

[Kim00] N. Kim *et al*, *Phase-coherent conduction in mesoscopic normal-metal/superconductor hybrid junctions.*
Solid State Comm. **115**, 29 (2000)

[Kit96] C. Kittel, *Introduction to Solid State Physics.* (John Wiley & Sons, Inc., 1996)

[Levi98] Y. Levi *et al*, *Scanning tunneling miscroscope studies of the superconductor proximity effect.* Phys. Rev. B **58**, 15128 (1998)

[Maz99] I.I. Mazin, *How to Define and Calculate the Degree of Spin Polarization in Ferromagnets.* Phys. Rev. Lett. **83**, 1427 (1999)

[Mes94] R. Meservey and P.M. Tedrow, *Spin-Polarized Electron Tunneling.*
Phys. Rep. **238**, 173 (1994)

[Moo95] J.S. Moodera *et al*, *Large Magnetoresistance at Room Temperature in Ferromagnetic Thin Film Tunnel Junctions.* Phys. Rev. Lett. **74**, 3273 (1995)

[Nad00] B. Nadgorny *et al*, *The origin of high transport spin polarization in* $La_{0.7}Sr_{0.3}MnO_3$*: direct evidence for minority spin states.* Phys. Rev. B **63**, 184433 (2001)

[Pob96] F. Pobell, *Matter and methods at low temperatures.* (Spinger, 1996)

[Pri95] G.A. Prinz, *Spin-Polarized Transport.* Physics Today **48**, 58 (1995)

[Rei65] F. Reif, *Fundamentals of statistical and thermal physics.* (McCraw-Hill Inc., 1965, chapter 13)

[Ros78] A.C. Rose-Innes and E.H. Rhoderick, *Introduction to superconductivity.* (Pergamon, 1978, chapter 9-10)

[Sha65] Y.V. Sharvin, Zh. Eksp. Teor. Fiz. **48**, 984 (1965)

[Sou98] R.J. Soulen Jr. *et al*, *Measuring the Spin Polarization of a Metal with a Superconducting Point Contact.* Science **282**, 85 (1998)

[Strij99] G.J. Strijkers, *Magnetic Nanostructures: An experimental study of structural, magnetic and transport properties.* (Ph.D. thesis, Eindhoven University of Technology, Eindhoven, 1999); Chapter 1.

[Strij01] G.J. Strijkers *et al*, *Andreev reflections at metal/superconductor point contacts: Measurement and analysis.* Phys. Rev. B **63**, 104510 (2001)

[Ted73] P.M. Tedrow and R. Meservey, *Spin Polarization of Electrons from Films of Fe, Co, Ni, and Gd.* Phys. Rev. B **7**, 318 (1973)

[Tink96] M. Tinkham, *Introduction to Superconductivity.* (McGraw-Hill, New York, 1996)

[Upad98] S.K. Upadhyay *et al*, *Probing Ferromagnets with Andreev Reflection.* Phys. Rev. Lett. **81**, 3247 (1998)

[West99] P.S. Westbrook and A. Javan, *Finite-bias resistance peaks in nanoscale superconductor-normal-metal Ta-W point contacts.* Phys. Rev. B **59**, 14606 (1999)

[Xiong98] P. Xiong, G. Xiao and R.B. Laibowitz, *Subgap and Above-gap Differential Resistance Anomalies in Superconductor-Normal-Metal Microjunctions.* Phys. Rev. Lett. **71**, 1907 (1993)